Volume 3
Number 4
April 2025
Pages 1587–1984

RSC Sustainability

rsc.li/rscsus

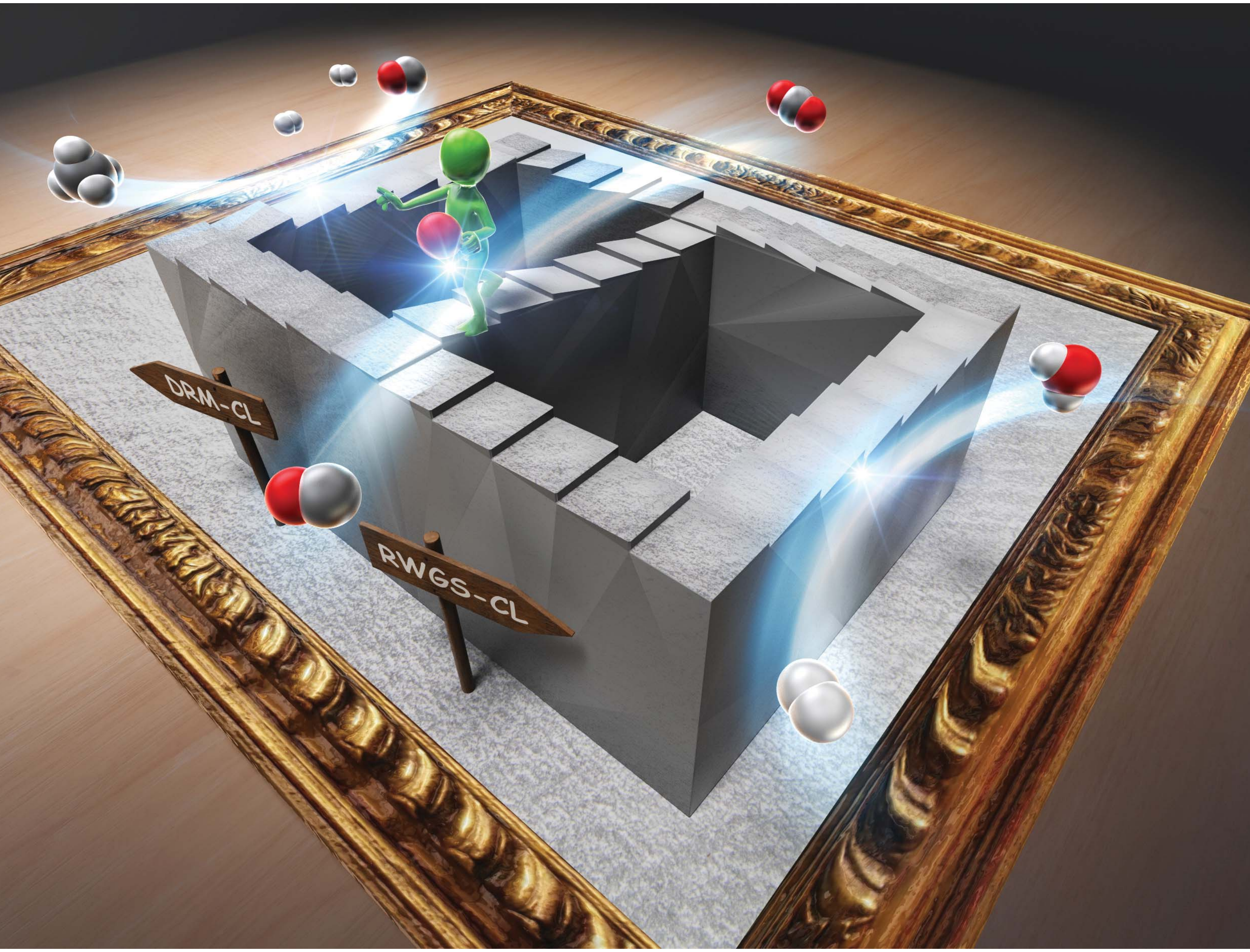

ISSN 2753-8125

ROYAL SOCIETY OF CHEMISTRY

CRITICAL REVIEW
Yasushi Sekine *et al.*
CO_2 conversion to CO by reverse water gas shift and dry reforming using chemical looping

RSC
Sustainability

ROYAL SOCIETY
OF CHEMISTRY

CRITICAL REVIEW

View Article Online
View Journal | View Issue

Check for updates

Cite this: *RSC Sustainability*, 2025, **3**, 1598

CO_2 conversion to CO by reverse water gas shift and dry reforming using chemical looping†

Keke Kang,‡ Hiroshi Sampei ‡ and Yasushi Sekine *

Chemical looping technology provides an efficient means of sustainable CO_2 conversion to the important chemical intermediate of CO or syngas by changing conventional co-feeding of reactant into alternating feeding. It presents the important benefits of simplified gas separation, improved selectivity, and more independently adjusted operation conditions compared to those of conventional reactions. Oxygen carriers (OCs) are pivotally important for the performance of chemical looping processes. Herein, recent advances of OCs for two representative chemical looping CO_2 conversion technologies to CO are reviewed systematically: reverse water gas shift chemical looping (RWGS-CL) and dry reforming of methane by chemical looping (DRM-CL). The influence of composition along with surface and bulk structures of these OCs on conversion, selectivity, and lattice oxygen reactivity, are discussed to obtain better design and optimisation strategies for the tailored OCs. Moreover, modified Ellingham diagrams that exhibit the thermodynamic properties for potential metal oxides for the effective screening of active OCs of DRM-CL and RWGS-CL are proposed, yielding valuable insights not only into RWGS-CL and DRM-CL but also into other distinct chemical looping processes involving into the same reactions. Finally, a summary and prospects are presented for some challenges and future research orientation for CO_2 conversion to CO *via* chemical looping.

Received 18th July 2024
Accepted 6th January 2025

DOI: 10.1039/d4su00395k

rsc.li/rscsus

Sustainability spotlight

Chemical looping technology provides an efficient means of continuously converting CO_2 into CO or synthesis gas, which are important chemical intermediates or fuels, by changing the conventional co-feeding of reactants to alternate feeding. Compared to conventional catalytic reactions, it has the important advantages of simplifying gas separation, improving selectivity, and allowing more independent adjustment of operating conditions. By continuing to research oxygen carriers (OC) for this purpose, it will be possible to efficiently recycle the carbon dioxide and biogas (a mixture of carbon dioxide and methane) that are emitted. These correspond to SDGs 7, 12, and 13.

1. Introduction

With the progressing development of industry worldwide, fossil fuels are increasingly used widely, entailing excessive emissions of carbon dioxide (CO_2). Incessantly, CO_2 concentrations in the atmosphere reach record high levels. Their continued growth is leading to important environmental difficulties such as global warming, rising sea levels, and ocean acidification.[1,2] As a result, environmentally friendly and economical means of CO_2 elimination are sought. Consequently, to create a carbon-neutral human society, carbon capture and utilisation (CCU) technologies with a sustainable carbon cycle have been developed extensively.[3–7]

Serving as the foundation of C1 chemistry, carbon monoxide (CO) is an important raw material for the synthesis of many organic chemical products and intermediates. Almost all basic chemicals such as phosgene, alcohol, acid, anhydride, ester, aldehyde, ether, amine, alkanes, and olefin are producible from CO.[8,9] As a major component of syngas, CO is necessary for gas-to-liquid conversion *via* the Fischer–Tropsch (F–T) process.[10–14] Liquid fuels possess characteristics of stable and high calorific value, non-volatility or low-volatility, and higher safety.[12–15] Therefore, sustainable CO_2 conversion, which successfully combines CO_2 reduction with the production of alternative liquid fuels, is regarded as a promising CCU technology.

A representative means of "CO_2 to CO" conversion is the reverse water–gas shift (RWGS) reaction, a non-fossil process, which uses renewable H_2 over a suitable catalyst according to eqn (1). However, CO_2 conversion *via* RWGS is limited by equilibrium because of its reversible nature. Furthermore, higher temperatures must be used for RWGS because of the reactions' endothermic nature and pressure independence, which are not conducive to connection with F–T processes at low temperatures to use the produced CO or to use various promising catalysts with a lower melting point.[16,17] Furthermore, the unwanted side reactions of methanation in eqn (2)

Waseda University, Tokyo, Japan. E-mail: ysekine@waseda.jp

† Electronic supplementary information (ESI) available. See DOI: https://doi.org/10.1039/d4su00395k

‡ K. K. and H. S. contributed equally.

and (3) always proceed in the RWGS process. They are exothermic, providing poor selectivity at lower temperatures with the production of methane (CH_4) instead of CO.[17] Furthermore, the CH_4 by-product leads to more complicated gas separation. In summary, the development of conventional RWGS is hindered severely by shortcomings such as equilibrium limitation, low energy efficiency, unwanted side reactions, and complex gas separation.

$$H_2 + CO_2 \leftrightarrow H_2O + CO,\ \Delta_r H^\theta\ (298\ \text{K}) = 41.2\ \text{kJ mol}^{-1} \quad (1)$$

$$CO_2 + 4H_2 \leftrightarrow CH_4 + 2H_2O,\ \Delta_r H^\theta\ (298\ \text{K}) = -165.0\ \text{kJ mol}^{-1} \quad (2)$$

$$CO + 3H_2 \leftrightarrow CH_4 + H_2O,\ \Delta_r H^\theta\ (298\ \text{K}) = -206.2\ \text{kJ mol}^{-1} \quad (3)$$

Dry reforming of methane (DRM) described in eqn (4) is another widely investigated method for "CO_2 to CO" conversion because it can convert main greenhouse gases of two kinds (CO_2 and CH_4) into industrially valuable syngas simultaneously over appropriate catalysts. However, DRM is an endothermic reaction. The catalysts used to date are composed mainly of expensive noble metals. Moreover, the intrinsic activity of the DRM process is not so high. The side reactions of RWGS entail the co-existence of CO_2 and H_2, leading to a lower syngas ratio than expected from the DRM process.[18,19] Importantly, carbon deposition, caused mainly by CH_4 decomposition and the Boudouard reaction (eqn (5) and (6)), deactivate the catalysts severely at lower temperatures.[20] These shortcomings strongly hinder the wider application of DRM.

$$CH_4 + CO_2 \rightarrow 2CO + 2H_2,\ \Delta_r H^\theta\ (298\ \text{K}) = 260.5\ \text{kJ mol}^{-1} \quad (4)$$

$$CH_4 \rightarrow C + 2H_2,\ \Delta_r H^\theta\ (298\ \text{K}) = -74.1\ \text{kJ mol}^{-1} \quad (5)$$

$$2CO \rightarrow CO_2 + C_{(s)},\ \Delta_r H^\theta\ (298\ \text{K}) = -172.5\ \text{kJ mol}^{-1} \quad (6)$$

One method to improve these two conventional "CO_2 to CO" processes (RWGS and DRM) is chemical looping (CL),[21,22] whereby one reaction is divided into several sub-reactions that can proceed in segregated steps and sites. Oxygen carriers (OCs) act as important intermediates, recycling the CL reaction by releasing and receiving the oxygen continuously. As exhibited in Fig. 1(a), the CL processes consist of reduction and oxidation steps that can proceed in individual conditions and spaces. During the reduction step, metal oxides (MO_x) acting as OCs are reduced with the oxygen released. In addition, H_2 is oxidised to H_2O in RWGS-CL (eqn (7), green in Fig. 1(a)); CH_4 is partially oxidised to CO and H_2 in the DRM-CL (partial oxidation of methane (POM) reaction in eqn (8), blue in Fig. 1(a)). Subsequently, during the common oxidation step of RWGS-CL and DRM-CL, $MO_{x-\delta}$ is regenerated back to MO_x by CO_2 with CO production (CO_2 splitting reaction in eq. (9), black in Fig. 1(a)). Reduction and oxidation proceed step by step in CL, bringing several great benefits over those provided by conventional processes. First, the reactant and product gas are inherently separated, avoiding some side reactions, simplifying gas separation, and greatly improving safety. Moreover, the equilibrium barrier of the conventional processes can be circumvented by CL

Keke Kang

Keke Kang, PhD, Keke Kang obtained her Master's degree in Environmental Science from the Chongqing Institute of the University of Chinese Academy of Sciences in 2021. Subsequently, under the guidance of Prof. Sekine, she completed her PhD at Waseda University in Japan in 2024. Her research interests span chemical looping for the conversion of CO_2 into syngas and the NH_3-SCR method for denitrification.

Hiroshi Sampei

Hiroshi Sampei, Mr, Hiroshi Sampei (Japan, 1998) received his MEng from Waseda University in 2023. He joined the PhD program at Waseda University with the group of Prof. Sekine in 2023. His research interests include precise surface modeling, mechanisms of heterogeneous catalysis by combination of theory and experiments, material design using computational methods, and topics related to computational catalysis.

Yasushi Sekine

Yasushi Sekine, PhD, FRSC, Prof., Waseda University, Tokyo, Japan, Yasushi Sekine (b. 1968), PhD from The University of Tokyo 1998, became professor at Department of Applied Chemistry, Waseda Univ. 2012. He works with low-temperature catalysis, specialising in protons and protonic transport in oxides and on their surfaces. Sekine has published 235 journal papers, supervised 112 Master- and 15 PhD-students, and is a fellow of RSC (FRSC) and a member of other national academies.

with repeated cycles of reduction and oxidation, thereby breaking the thermodynamic restraints and further improving the reaction potential using optimal conditions for each step. As a result, CL processes are promising options for effective CO_2 and CH_4 usage. Fig. 1(b) exhibits the overall concept with RWGS-CL or DRM-CL to produce synthesised gas of xH$_2$ + yCO, yielding valuable and diverse chemicals. F–T fuels (hydrocarbons) and methanol are producible with a syngas ratio (H_2/CO) of 2, whereas the production of dimethyl ether (DME) and oxo-alcohols (adding olefins) relies on CO-rich syngas. Furthermore, the production of NH_3 and acetic acid respectively requires H_2 and CO.[20]

$$MO_x + H_2 \rightarrow MO_{x-\delta} + H_2O \tag{7}$$

$$MO_x + CH_4 \rightarrow MO_{x-\delta} + CO + 2H_2 \tag{8}$$

$$MO_{x-\delta} + CO_2 \leftrightarrow MO_x + CO \tag{9}$$

Actually, OCs are fundamentally important for CL processes. Appropriate OCs require qualified activity to the reactants both during the reduction and oxidation steps, high selectivity to target products, excellent resistance to sintering, carbon deposition and abrasion, as well as low cost. Recently, many efforts have been undertaken to develop appropriate OCs with superior performance for CL. In fact, several excellent reviews have assigned emphasis to the OCs of CL emerged.[21,23–30] However, those reviews mainly overviewed chemical looping combustion (CLC) and chemical looping reforming (CLR) related topics: no investigation specifically examined CO_2 conversion to CO *via* CL. Furthermore, while the history and overview of CCUs by chemical loops have been summarized so far, no review focusing on materials has been done so far.[31,32] Therefore, this review particularly assesses recent advances in OC development on CO_2 conversion to CO *via* chemical looping (mainly RWGS-CL and DRM-CL). After first reviewing recently developed OCs (*e.g.*, perovskites, spinels, metal-based oxides) on RWGS-CL and DRM-CL, we calculate and then present a summary of the thermodynamic properties of potential metal oxides in the modified Ellingham diagrams for the screening of active OCs for CL processes. Finally, the main conclusion and prospects for meeting some challenges and future research orientation are introduced.

2. Reverse water gas shift chemical looping (RWGS-CL)

Actually, RWGS-CL can produce CO from CO_2 without by-products and with superior energy efficiency to that of the conventional RWGS process. The side reaction of methane formation (eqn (2) and (3)) is avoided. Moreover, gas separation for produced CO is simplified by avoiding the simultaneous introduction of carbon and hydrogen species. A recent research report has described the conversion of CO_2 to liquid fuel *via* RWGS (at 1250 K and 30 atm) using solar energy.[4] The provision of H_2 consumes the most energy by heating the reactor and power electrolysers to the target temperature. The use of H_2 can be reduced in RWGS-CL because stoichiometric reactions are feasible, without requiring excess H_2 to satisfy kinetic and thermodynamic considerations, making it more economically feasible. Furthermore, the operational temperatures for the reduction step in RWGS-CL are lower because of the thermochemical characteristics, typically 673–1223 K. Moreover, some OCs can operate under isothermal conditions.[33–36]

The key aspect of the RWGS-CL process is the choice of oxygen carrier able to strike a balance between the reduction conducted using a strong reducing agent of H_2 and the oxidation driven by a weak oxidising agent of CO_2. This balance enables both steps to take place at the same temperature, which can cut the inefficiency arising from different operation temperatures during cycling. Furthermore, operating at lower temperatures is fundamentally important because it aligns with the lower temperature requirements for some downstream processes such as methanol and Fischer–Tropsch synthesis, which can be conducted at temperatures lower than 623 K.[14] Furthermore, running at lower temperatures enables the use of more cost-effective materials such as

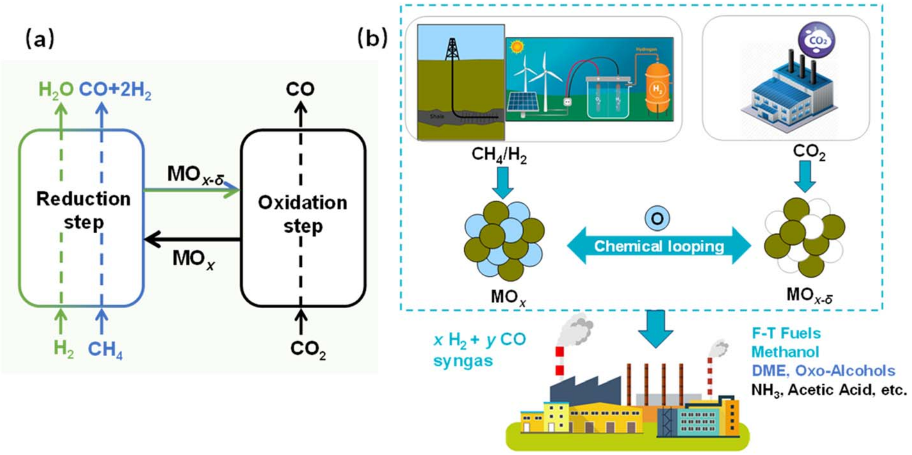

Fig. 1 (a) Schematic diagram of RWGS and DRM by chemical looping and (b) overall concept with RWGS-CL or DRM-CL.

Table 1 CO_2 splitting of composite OCs for RWGS-CL

OCs	CO_2 concentration/%	Space velocity/L min^{-1} g^{-1}	Temperature/K	CO yield/mmol g^{-1}	Average CO_2 splitting rate[a]/μmol g^{-1} min^{-1}	Reference
$LaCo_{0.25}Fe_{0.5}Mn_{0.25}O_3$	10.0	0.67	873	0.90	N/A	Ramos *et al.*[37]
$La_{0.75}Sr_{0.25}CoO_{3-\delta}$	10.0	N/A	923	N/A	14.7 (673 K); 38 (773 K); 20.6 (873 K)	Daza *et al.*[35]
			1023		65.7 (673 K); 98.4 (773 K); 73.4 (873 K)	
			1123		146.3 (673 K); 172.6 ± 17.4 (773 K); 198.1 (873 K)	
$La_{0.75}Sr_{0.25}FeO_{3-\delta}$ (LSF)	6.7	0.67(CO_2/He), 0.65(H_2/He)	823	0.74–1.09	77.2	Daza *et al.*[36]
LSF/SiO_2	10.0	0.67	873	2.60	800.0	Hare *et al.*[40]
LSF/SBA-15	100.0	0.05	873	2.80	150.0	Jo *et al.*[42]
Cu/LSF	N/A	0.67	823	N/A	61.3–69.7	Daza *et al.*[45]
NiO@LSF	10.0	0.50	873	1.15	N/A	Lee *et al.*[46]
Co_3O_4@LSF				1.45		
Co_3O_4–NiO@LSF				1.60		
CeO_2@LSF				0.55		
LSF				0.35		
$La_{0.4}Ba_{0.6}FeO_3$	10.0	0.67	773	0.50	N/A	Shi *et al.*[49]
$La_{0.5}Ba_{0.5}FeO_3$				0.20		
$La_{0.25}Ba_{0.75}FeO_3$				0.19–1.5		
$La_{0.5}Ba_{0.5}FeO_3/SiO_2$	10.0	0.17	823	2.20	220.0	Shi *et al.*[50]
La_2NiFeO_6	25.0	0.50	973	2.14	214.0	Lim *et al.*[51]
$Cu_{0.4}Co_{0.6}Fe_2O_4$	20.0	1.60	823	N/A	98.3	Qiu *et al.*[52]
			923	9.10	144.6	
			1023	10.50	347.8	
			1123	11.20	493.1	
$CoFe_2O_4$	20.0		923	7.30	112.5	
			1023	9.20	N/A	
			1123	10.00	N/A	
$Ni_{0.4}Co_{0.6}Fe_2O_4$	20.0		923	6.60	99.7	
			1023	8.60	N/A	
			1123	9.50	N/A	
$Mn_{0.4}Co_{0.6}Fe_2O_4$	20.0		923	4.40	70.6	
			1023	6.00	N/A	
			1123	7.00	N/A	
$Mn_{0.2}Co_{0.8}Fe_2O_4$	20.0	1.60	823	N/A	100.0	Ma *et al.*[53]
			923	8.80	142.3	
			1023	N/A	310.0	
			1123	N/A	500.0	

[a] Temperatures in brackets show different reduction temperatures before the CO_2 splitting step.

stainless steel in the reactor. Moreover, it is desirable to maintain the structural stability of OCs because, in many cases, less energy is required to refill the lattice oxygen than to restore the crystalline structure. These facts underscore the important task of developing RWGS-CL OCs that can accommodate the creation of plenty of oxygen vacancies effectively, exhibit suitable kinetics for CO_2 activation and oxygen exchange, and maintain their structural integrity throughout multiple reaction cycles. Actually, in recent years, OCs with diverse active metals, inert supports, and various preparation methods have been screened and selected. Tables 1 and 2 present the CO_2 splitting performance of OCs for RWGS-CL reported in the reviewed literature.

2.1 Composite oxide

Composite oxides with stoichiometric composition and special structures such as perovskites and spinel oxides were investigated widely for RWGS-CL because of their adaptable and stable structures. Table 1 presents a summary of the CO_2 splitting performance data of composite OCs in recent reports for RWGS-CL.

2.1.1 Perovskites (ABO_3). Perovskite oxides (ABO_3) exhibit versatile redox characteristics because of their substitutable A and B sites, reversible oxygen storage, and high structural stability. These features make them excellent candidates for developing innovative composite oxides for the RWGS-CL process. For instance, Ramos *et al.* concurrently doped transition metals (Co, Fe) into the B site of the $LaMnO_3$ structure.[37] Their DFT findings highlight the potential of the Fe-rich sample to support isothermal RWGS-CL and to produce CO without decomposition. Whereas Mn and Co-rich samples formed oxygen vacancies, the Co-rich sample presented difficulties because of its susceptibility to decomposition during RWGS-CL. Additionally, the improved CO_2 conversion performance was found to be related closely to the large surface areas provided by the small crystallite sizes. Undertaking a similar pursuit, Daza and colleagues initially explored $La_{0.75}Sr_{0.25}CoO_{3-\delta}$ as a parent material for RWGS-CL, which was transformed to layered perovskite ($La_{2-y}Sr_yCoO_4$) after the first redox cycle because of its weak oxidation ability with CO_2.[35] After H_2 reduction, the oxide phases were changed into metallic cobalt and base oxides. They were subsequently regenerated back to the layered perovskite after CO_2 reoxidation. Nevertheless, this layered perovskite was not stable when contacting with CO_2. Furthermore, it required different oxidation and reduction temperatures, with the optimal operational temperature remaining high: 1123 K. Furthermore, the best oxidation temperature was related closely to the close contact of $La_{2-y}Sr_yCoO_4$ and Co. Therefore, their research group later introduced $La_{0.75}Sr_{0.25}FeO_{3-\delta}$ (LSF) as a more promising alternative.[38] As Fig. 2(a) and (b) show, LSF exhibited remarkable redox properties, facilitating isothermal operation at the lower temperature of 823 K while maintaining structural stability. Furthermore, its excellent CO_2 splitting performance can be attributed to the strengthened adsorption of CO_2 attributable to the increased oxygen vacancies (Fig. 2(c)).

Because LSF combines the low energy barrier for oxidation-state transitions (Fe^{3+}–Fe^{2+}) during redox cycles,[39] the CO_2 affinity facilitated by the slight basicity of La,[40] and the enhanced lattice oxygen diffusion from a subtle oxygen

Table 2 Summary of CO_2 splitting performance of metal based-OCs for RWGS-CL

OCs	CO_2 concentration/%	Space velocity/ L min^{-1} g^{-1}	Temperature/K	CO yield/ mmol g^{-1}	Average CO_2 splitting rate/ μmol g^{-1} min^{-1}	CO_2 conversion/%	Reference
$Fe_{0.35}Ni_{0.65}O_x$	100.0	1.25^a(H_2), 0.75^a(CO_2)	773	3.20	N/A	N/A	Rojas *et al.*[54]
Fe_3O_4–$Ce_{0.5}Zr_{0.5}O_2$	50.0	1.00	1073	1.00	22.2	N/A	Wenzel *et al.*[55]
Fe_2O_3–$LaFeO_3$	20.0	0.50	750	12.10	605.0	N/A	Lee *et al.*[56]
$Fe_2O_3/Gd_{0.1}Ce_{1.9}O_{2-\delta}$	10.0	0.40	1023	N/A	693.0	38.8	Zeng *et al.*[57]
$Fe_2O_3/Gd_{0.2}Ce_{1.8}O_{2-\delta}$				N/A	728.0	40.8	
$Fe_2O_3/Gd_{0.3}Ce_{1.7}O_{2-\delta}$				10.79	770.0	43.2	
$Fe_2O_3/Gd_{0.5}Ce_{1.5}O_{2-\delta}$				N/A	719.0	40.3	
Cu–In_2O_3	10.0	N/A	673	2.90	58.7	30.0	Makiura *et al.*[58]
			723	3.79	115.0	35.0	
			773	4.80	161.8	30.0	
			823	N/A	340.0	30.0	
			873	N/A	457.0	32.5	
Co–In_2O_3	10.0	N/A	723	1.62	127.6	80.0	Makiura *et al.*[60]
			748	2.29	191.0	N/A	
			773	3.27	280.2	80.0	
			798	4.14	365.7	N/A	
			823	5.15	429.5	N/A	
$NiGa_2O_x$	10.0	N/A	973	4.05	367.4	99.0	Kang *et al.*[59]
$CuGa_2O_x$				0.80	160.7	99.0	
$CoGa_2O_x$				2.72	138.5	99.0	

[a] The maximum weight of OCs is used for calculation, despite there is a weight range.

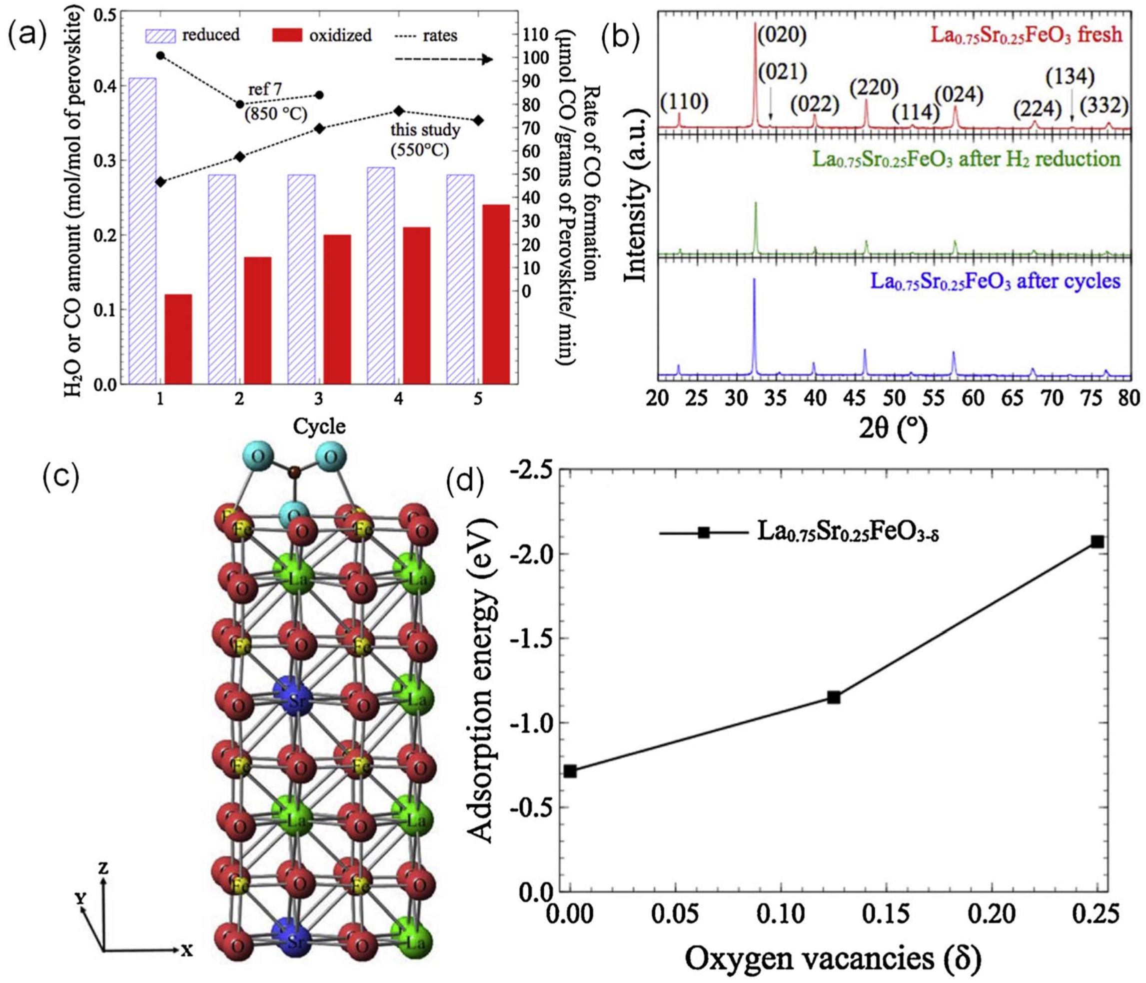

Fig. 2 (a) RWGS-CL performance of $La_{0.75}Sr_{0.25}FeO_3$ (LSF) at 823 K. (b) XRD data of the LSF powder during RWGS-CL. (c) Adsorption energies of CO_2 on (1 0 0) facet of stoichiometric LSF. (d) Change of CO_2 adsorption energy with oxygen vacancies ($\delta = 0$, 0.125, 0.250). Reprinted with permission.[38] Copyright 2014 Elsevier.

deficiency induced by moderate Sr doping,[41] it has shown high industrial potential for RWGS-CL. Therefore, some related research work has contributed to the improvement of LSF by introducing additional components, specifically supports and metals, by changing the introduction method, and by designing the particle structure. Hare *et al.* identified SiO_2 as superior support when compared to CeO_2, ZrO_2, Al_2O_3, and TiO_2 for LSF in RWGS-CL, enhancing the CO yield of pure LSF by 150%.[42] This better support can be attributed primarily to the decreased perovskite particle size and crystallite size facilitated by SiO_2. Furthermore, despite the observation of minor secondary phases at the LSF-support interface, the perovskite oxide phase remained active in generating oxygen vacancies. Subsequently, they reported other work conducted by loading 25 wt% LSF onto SiO_2, which yielded impressive performance by increasing the CO yield of LSF by approximately 200% during eight RWGS-CL cycles.[33] These enhancements were attributed to the lattice strain associated with SiO_2 support and the decreased secondary phases which might obstruct access to active surfaces, in addition to the decreased particle and crystallite size. Brower and colleagues advanced this line of research by introducing high-surface-area mesoporous SiO_2 (SBA-15) support to LSF using two methods.[43] The first approach involved the addition of the LSF to SBA-15 through a sonication process using wet SiO_2 (SWS process), which increased the surface area and pore volume considerably. However, this approach presented a challenge to the maintenance of the desired perovskite stoichiometry because of the presence of secondary phases containing Sr-based oxides. In contrast, the second method incorporated SBA-15 during the sol–gel stage of perovskite oxide formation (ASG process), proving to be more effective at ensuring structural stability, improving CO yields, and increasing surface area and pore volume. Results show that the ASG-synthesised composite with 50% loading of LSF increased the total surface area by approx. 300% and enhanced the CO yields by a factor of 10 compared to pure LSF in six redox cycles at 973 K. Furthermore, Jo and his team used a nanocasting method to synthesise mesoporous LSF and then explored the effects of controlled template removal from the nanocast LSF on its textural properties and redox reactivity.[44] As

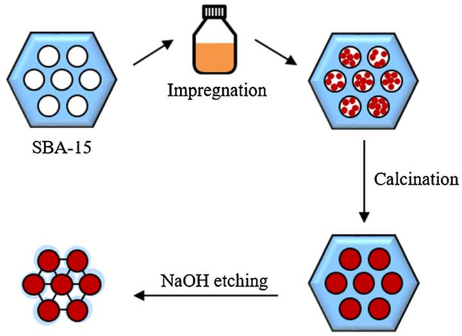

Fig. 3 Synthesis method of nanocast mesoporous LSF. Reprinted with permission.[44] Copyright 2021 Elsevier.

depicted in Fig. 3, LSF was impregnated initially onto SBA-15, a mesoporous silica template, with subsequent template removal through NaOH etching. The decreased residual Si content led to dramatic enhancements in specific surface area, total pore volume, and metal dispersion, but the mesoporous structure collapsed when the Si content became lower than 5 wt%. Moreover, maintaining a specific Si content was important to maintain the atomic ratio of surface oxygen to lattice oxygen to achieve peak CO productivity. Ultimately, mesoporous LSF with optimal Si content of 10 wt% achieved an impressive average CO yield of 2.80 mmol g^{-1} for RWGS-CL at 873 K, surpassing that of bulk LSF by a factor of 5.9. Daza and his team, after incorporating Cu in the B site of LSF, found that only perovskites with the lowest Cu substitution of 0.1 and those devoid of Cu exhibited the unique capability to produce CO.[45] This finding is explainable: Cu incorporation altered the oxygen affinity of LSF structure and limited its ability to be re-oxidised using CO_2. Minbeom and colleagues explored the potential of metal oxide core–perovskite shell OCs for the RWGS-CL process by preparing and testing LSF and MeO_x@LSF (MeO_x: CeO_2, NiO, Co_3O_4, and Co_3O_4–NiO).[46] Cyclic RWGS-CL experiments demonstrated that NiO@LSF, Co_3O_4@LSF, and Co_3O_4–NiO@LSF enhanced the LSF performance. Additionally, CeO_2@LSF exhibited a similar performance to that of LSF because of the low oxygen capacity of CeO_2. Actually, Co_3O_4–NiO@LSF, which maintained stable CO production over 20 cycles, emerged as an optimal OC because it combined the benefits of both Co_3O_4@LSF and NiO@LSF. Furthermore, the investigated core–shell-structured OCs can form and consume oxygen defects efficiently, even at lower temperatures.

Apart from LSF, $La_{1-x}Ba_xFeO_3$ (LBF) was also identified from DFT calculation and stable structures indicated by proper Goldschmidt tolerance factor as a promising OC because of its comparable oxygen vacancy formation energy to that of LSF.[47,48] Shi *et al.* prepared LBF ($x = 0.25$–0.75) perovskites for efficient and stable CO production by RWGS-CL.[49] Their findings show that $La_{0.25}Ba_{0.75}FeO_3$ exhibited efficient CO production but faced partial decomposition, whereas $La_{0.5}Ba_{0.5}FeO_3$ exhibited excellent stability, but only after inefficient CO production. A balance between stability and yield was struck with $La_{0.4}Ba_{0.6}FeO_3$, which showed high stability and efficient CO production at the low temperature of 773 K. The enhanced stability and lowered reaction temperature were attributed to La on the A site, whereas the increased CO production was attributed to the introduction of Ba. The surface oxidation mechanism was inferred as the following: CO_2 was adsorbed onto the reduced surface, forming carbonates even at room temperature, which were dissociated into C–O and O at temperatures higher than 523 K. The dissociated C–O and O desorbed at temperatures higher than 773 K, respectively producing CO and regenerating the LBF to its initial state. Shi and his team further explored the potential of 25 wt% $La_{0.5}Ba_{0.5}FeO_3$ supported on SiO_2 for industrial use for RWGS-CL.[50] Their results indicate that the CO_2 adsorption was enhanced from 18.3 to 62.2 μmol g^{-1} LBF by introducing the SiO_2 support, which increased CO production from 0.2 to 2.2 mmol g^{-1} LBF. To ensure industrial applicability, SiO_2-supported $La_{0.5}Ba_{0.5}FeO_3$ was processed into high-strength pellets using optimised tabletting and extrusion methods. The CO_2 oxidation temperature of LBF/SiO_2 pellets was 823 K, which was 50 K higher than that of LBF. The redox performance of all pellets remained stable throughout 50 cycles of semi-batch reactor tests. Additionally, deactivated pellets can be regenerated through thermal treatment with air.

Recently, double perovskite structures ($A_2BB'O_6$) have also garnered extensive attention because of their synergistic interaction and induced distortion in BO_6 octahedra by the incorporation of different B and B′ cations. Lim *et al.* synthesised a double perovskite of La_2NiFeO_6 to elucidate the role of interaction between binary Ni and Fe sites in enhancing CO_2 conversion when compared to single $LaNiO_3$ and $LaFeO_3$ perovskites.[51] The Ni site played a pivotal role in facilitating hydrogen atom adsorption, the formation of surface oxygen vacancies, and the transfer of lattice oxygen. Additionally, the Ni site promoted the poor reduction of Fe cations. Furthermore, the Fe site prevented the strong adsorption of CO_2 molecules on the La sites, facilitating their direct dissociation into CO molecules on the oxygen vacant sites or the reduced transition metal sites. The incorporation of Fe into the B site of $LaNiO_3$ addressed the poor CO_2 splitting activity observed in the single $LaNiO_3$ perovskite. The double La_2NiFeO_6 perovskite emerged as a high-performing option, with an average CO productivity of 2.14 mmol g^{-1} and a maximum CO production rate of 1.69 mmol g^{-1} min^{-1} at 973 K, respectively surpassing those of single perovskites by factors of more than 4.7 and 10.

2.1.2 Spinels (AB_2O_4). In addition to perovskite, spinel is a viable family of metal oxides for OCs in RWGS-CL processes. Spinels' potential benefits derive from their adaptable and highly thermally stable crystal structure. In fact, both the A and B positions within their structures can be occupied by readily available Earth-abundant metals. Qiu *et al.* found that $Cu_{0.4}Co_{0.6}Fe_2O_4$ exhibits an impressive CO_2 splitting rate and total CO production even at moderate temperatures, which was attributed to the reduction ability of cobalt ferrite by doping Cu and the reversible phase change after CO_2 oxidation.[52] Furthermore, Ma *et al.* reported that $Mn_{0.2}Co_{0.8}Fe_2O_4$ exhibited the highest CO_2 splitting performance among all prepared OCs with a different doping amount of Mn at 923 K.[53] The enhanced redox activity might be attributed to the increased reduction depth during the reduction process and the high reversibility during CO_2 splitting. The decreased performance with higher levels of Mn doping was attributed to the low phase reversibility of the MnFe alloy.

2.2 Metal-based oxides

Metal-based oxides are attractive OCs for commercial-scale processes because of their accessibility and high oxygen storage capacities. However, because of their strong tendency to be sintered at a low temperature, deactivation of particles occurs easily. The OC performance cannot be maintained during long-term experimentation. Numerous research endeavours have been pursued to improve the performance of pure metal oxides by modifying and introducing other metal oxides, composite oxides, or supports. Table 2 presents a summary of the CO_2 splitting performance of metal-based OCs used in the following literature found for RWGS-CL.

2.2.1 Fe-based OCs. Iron oxides are promising because of their cost-effectiveness, environmental friendliness, and widespread availability. However, their limited activity at low temperatures and susceptibility to sintering at high temperatures pose challenges for industrial use. Numerous research efforts have been undertaken to improve the activity and the sintering resistance of iron oxides, with a notable emphasis on incorporating them with other metal oxides and depositing them onto refractory ESI.† Rojas *et al.* thermodynamically screened various ferrites using thermodynamic analyses and the calculation of phase diagrams (CALPHAD) simulations for RWGS-CL metal oxides.[54] They found that $Fe_{0.35}Ni_{0.65}O_x$ exhibits remarkable theoretical CO yield at 773 K (Fig. 4(a)). Moreover, its CO yield is closely related to the temperature and CO_2/CO ratio, as depicted in Fig. 4(b). A marked degree of 17.7% CO_2 conversion at 773 K was predicted, with a sharp increase in CO yield as the CO_2/CO ratio rises, indicating a phase change in the metal oxide. The 17.7% conversion prediction was subsequently validated through TGA experiments. The phase change was affirmed by the "sweet spot" marked by a stark discontinuity in molar enthalpy and entropy values in thermodynamic phase diagrams in Fig. 4(c) and by the important jumps in oxygen content plots in Fig. 4(d). Furthermore, as portrayed in Fig. 4(e), the redox performance of $Fe_{0.35}Ni_{0.65}O_x$ was compared with the $Mn_{0.4}Co_{0.6}Fe_2O_4$ spinel with the highest CO yield in an earlier report, revealing that $Fe_{0.35}Ni_{0.65}O_x$ exhibited higher oxygen capacity, CO yield, and stability at 773 K, which were attributed to the spinel-to-metallic phase transition.[53] Wenzel *et al.* introduced $Ce_{0.5}Zr_{0.5}O_2$ to modify pure Fe_2O_3: the 80 wt% Fe_2O_3–$Ce_{0.5}Zr_{0.5}O_2$ displayed stability over 500 redox cycles.[55] Despite experiencing initial deactivation in the first 100 cycles, subsequent cycling led to consistent CO yield per cycle over the remaining 400 cycles. The initial material deactivation resulted from surface sintering, which increased crystallite sizes and induced phase segregation into Fe-rich and Ce–Zr-rich regions. This phenomenon strongly affected the reaction kinetics and CO yield. The sintering of pure Fe_2O_3 can also be improved by adding perovskite. Lee *et al.* introduced a small quantity of $LaFeO_3$ into Fe_2O_3 for RWGS-CL, aiming to offer the high oxygen storage capacity of Fe_2O_3 and the redox stability of $LaFeO_3$.[56] In fact, Fe_2O_3–$LaFeO_3$ exhibited both increased CO yield and enhanced stability, with CO yield (12.1 mmol g^{-1}) and CO production rate (605 μmol g^{-1} min^{-1}) for 50 redox cycles at 750 K. The incorporation of $LaFeO_3$ perovskite served as a sintering barrier, preventing the migration of metallic cations between adjacent particles and alleviating the Kirkendall effect by changing the oxide growth direction. This strategic intervention mitigates structural deformations, thereby facilitating sustained CO_2 conversion. Moreover, the addition of $LaFeO_3$ enhances the electrical conductivity of the particles, facilitating the conduction of O^{2-}. In addition, to avoid a trade-off between reactivity and the stability caused by the addition of inert supports to Fe_2O_3, Zeng *et al.* proposed a novel approach using ion-conductive $Gd_xCe_{2-x}O_{2-\delta}$ (GDC) to prepare supported OCs.[57] The resulting Fe_2O_3/GDC materials exhibited both high reactivity and stability. Specifically, $Fe_2O_3/Gd_{0.3}Ce_{1.7}O_{2-\delta}$ showed remarkable CO productivity (approx. 10.79 mmol g^{-1}) and a high CO production rate (approx. 0.77 mmol g^{-1} min^{-1}), surpassing those of Fe_2O_3/Al_2O_3 by twofold, while maintaining stability over 30 cycles. The study also established a linear relation between O^{2-} conductivity and CO yield (Fig. 5(a)). This relation was validated using reference samples (Fig. 5(b)). The identified correlation served as a basis for predicting and designing OCs. However, its applicability under different conditions requires further investigation.

2.2.2 In-based and Ga-based OCs. In the authors' group, Makiura *et al.* prepared the parent material of $Cu_2In_2O_5$ using a complex polymerisation method, which was converted to the oxide structure consisting of reduced Cu supported on In_2O_3 (Cu–In_2O_3) after the first RWGS-CL cycle.[58] Cu–In_2O_3 showed superior CO_2 conversion at the low temperatures of 673–773 K and accomplished the RWGS-CL process by the redox of indium species accompanied by the formation and re-oxidation of Cu–In alloy. The structured state of Cu–In_2O_3 played an important role in its high oxidation performance, but the Cu-supported In_2O_3 and pure In_2O_3 prepared directly using an impregnation method exhibited only low performance. The excellent redox performance of Cu–In_2O_3 can be attributed to two characteristics: First, it has high reducibility by H_2, even at low temperatures, which was promoted by Cu species. Second, the Cu–In alloy particle surface has a highly reduced state maintained even when oxidised using CO_2, leading to its high CO_2 splitting rate. As depicted in Fig. 6, the interesting oxidation behaviour was attributed to rapid O^{2-} migration from the surface to the bulk of the Cu–In alloy and to the preferential oxidation of the interface between the alloy and In_2O_3. Although Cu–In_2O_3 showed outstanding kinetics performance, it still presents shortcomings such as poor stability and insufficient CO_2 conversion compared to conventional RWGS, which hinders its practical application.[59] Therefore, Makiura *et al.* later introduced another In-based material, Co–In_2O_3, which not only further improved the high CO_2 splitting rate of Cu–In_2O_3 at 723–823 K, but also remained stable even after 10 cycles.[60] Actually, it showed maximum CO_2 conversion of approximately 80%. This figure greatly exceeded the equilibrium conversion of catalytic RWGS in the mid-temperature range and efficiently decreased the cost for gas separation of CO_2 from the product gas of CO.

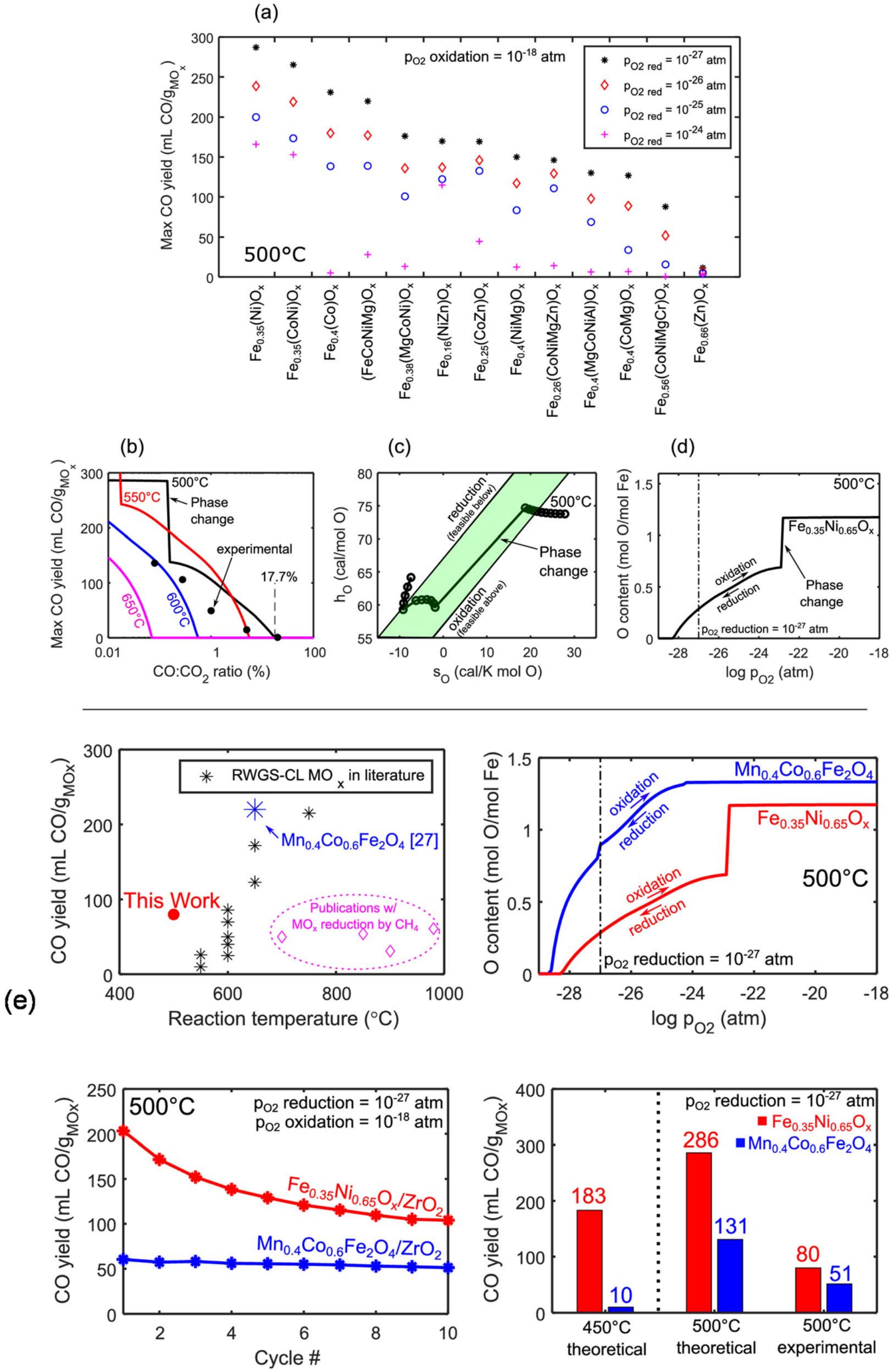

Fig. 4 Thermodynamic screening and verification by experimentation of RWGS-CL oxygen carriers. (a) Thermodynamic CO yield of promising RWGS-CL OC candidates with different reduction p_{O_2}. (b) Thermodynamic CO yield of $Fe_{0.35}Ni_{0.65}O_x$ with CO/CO$_2$ ratio as a function of temperature. (c) Thermodynamically calculated molar enthalpy with entropy plot of $Fe_{0.35}Ni_{0.65}O_x$. (d) Thermodynamically calculated oxygen content with p_{O_2} phase diagram of $Fe_{0.35}Ni_{0.65}O_x$ at 500 °C. (e) Comparison of $Fe_{0.35}Ni_{0.65}O_x$ to other reported RWGS-CL metal oxides. Reprinted with permission.[54] Copyright 2022 American Chemical Society.

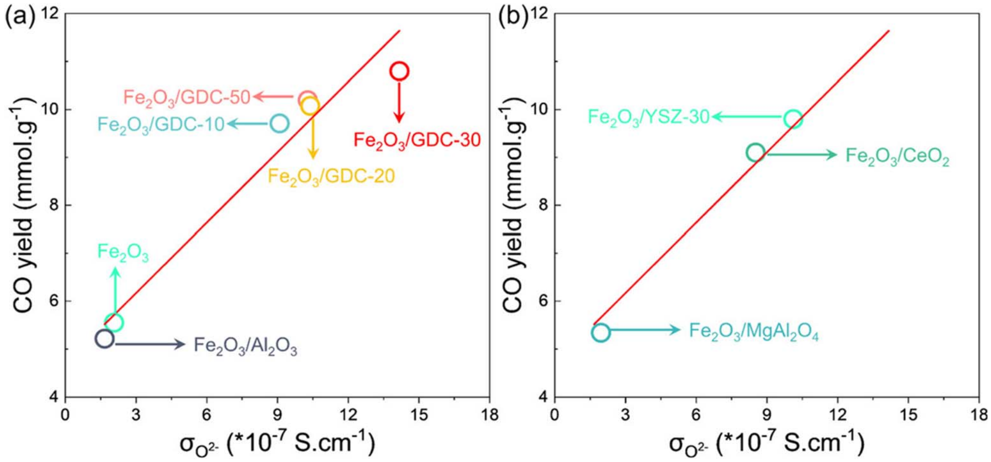

Fig. 5 (a) Fitted linear curve relation between O^{2-} conductivity and CO yield to predict activity of supported Fe_2O_3 and (b) O^{2-} conductivity and CO yield for reference samples to validate the fitted curves. Reprinted with permission.[57] Copyright 2020 American Chemical Society.

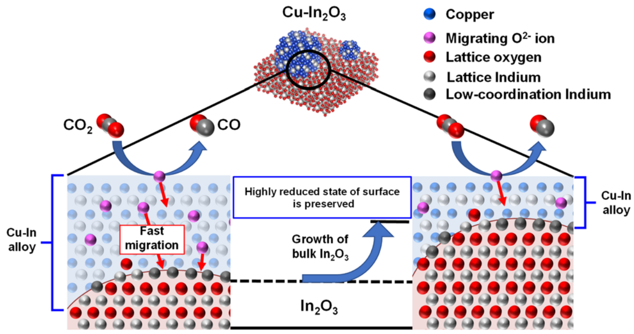

Fig. 6 Proposed mechanism of CO_2 splitting on the reduced Cu–In_2O_3. Reprinted with permission.[58] Copyright 2021 RSC Publishing.

However, the high splitting rate of Co–In_2O_3 was measured without the presence of CO. Moreover, the equilibrium CO_2 conversion can be improved further. To conserve energy and decrease costs further, Kang *et al.* developed MGa_2O_x (M = Ni, Cu, Co) materials, by which the RWGS-CL was able to achieve nearly 100% CO_2 conversion even when operated at temperatures as low as 673 K.[59] This high performance at a low temperature made it possible for RWGS to proceed without equilibrium constraints, even at low temperatures. Additionally, the CO_2 splitting rate and CO yield were evaluated with highly concentrated CO, which more closely matched the practical conditions. The results showed Ni to be a better dopant than either Co or Cu, which can be attributed to its excellent redox and CO adsorption abilities and to its large surface area. The redox cycle over $NiGa_2O_x$ was accomplished by the redox of $Ga^{3+} \leftrightarrow Ga^0$ with Ni in the metallic state through RWGS-CL, and by the presence of CO decreasing the CO_2 oxidation performance by restraining the oxygen amounts that can be re-filled by Ga species.

2.3 Summary and prospects for RWGS-CL

The reverse water gas shift chemical looping (RWGS-CL) process efficiently converts CO_2 into CO with lower energy requirements than conventional RWGS. It can be operated at moderate temperatures (673–1223 K) and aligns with downstream processes like methanol synthesis. Oxygen carriers (OCs) are crucial, enabling simultaneous reduction with H_2 and oxidation with CO_2.

Perovskites exhibit high oxygen storage and stability, enhanced by doping and structural modifications. Spinels show high CO yields. Doping and hybridization are effective for enhancing the durability of iron-based oxides. Cu–In_2O_3 is excellent at low temperatures and has efficient redox properties, but it has stability issues.

RWGS-CL has significant industrial potential thanks to its energy efficiency, lower operating temperatures, and adaptability. Continued innovation in OC development, including

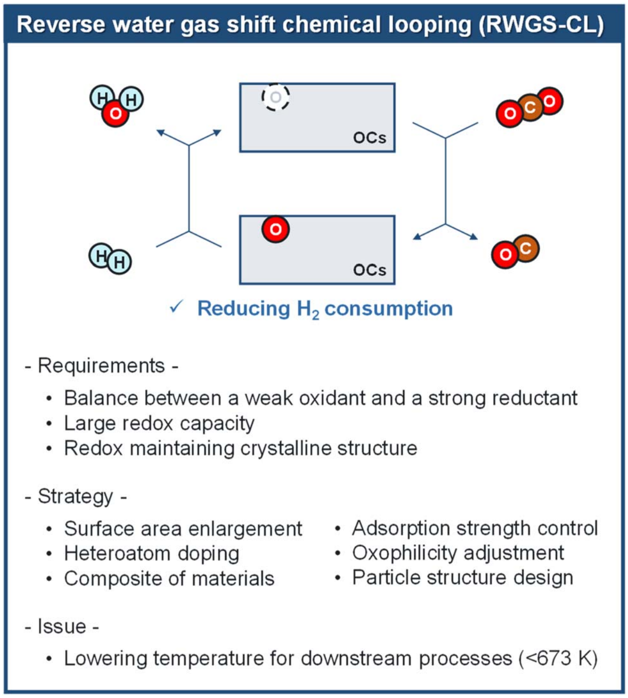

- Requirements -
- Balance between a weak oxidant and a strong reductant
- Large redox capacity
- Redox maintaining crystalline structure

- Strategy -
- Surface area enlargement
- Heteroatom doping
- Composite of materials
- Adsorption strength control
- Oxophilicity adjustment
- Particle structure design

- Issue -
- Lowering temperature for downstream processes (<673 K)

Fig. 7 Overview of material development for RWGS-CL.

Table 3 Summary of redox performance of composite OCs for DRM-CL

	Reduction step								Oxidation step				
OCs	Temperature/K	CH_4 concentration/%	Space velocity/L min^{-1} g^{-1}	*t*/min	CH_4 conversion/%	Syngas or CO selectivity/%	Syngas yield/mmol g^{-1}	CO_2 concentration/%	Space velocity/L min^{-1} g^{-1}	*t*/min	CO_2 conversion/%	CO yield/mmol g^{-1}	Reference
$LaFeO_3$	1123	10	0.10	4	26	57	1.20	10	0.10	4	19	0.32	Zhang *et al.*[64]
$La_{0.75}Ce_{0.25}FeO_3$					54	73	2.50				53	0.98	
$La_{0.5}Ce_{0.5}FeO_3$					83	90	4.20				92	1.65	
$La_{0.75}Ce_{0.25}FeO_3$					52	79	2.50				59	1.05	
$CeFeO_3$					10	55	0.44				5	0.08	
$LaFeO_3$	1123	5	0.20	30	N/A	N/A	10.05	5	0.20	30	N/A	5.00	Sastre *et al.*[65]
$La_{0.9}Sr_{0.1}FeO_3$					N/A	N/A	17.50				N/A	9.25	
$La_{0.7}Sr_{0.3}FeO_3$					N/A	N/A	15.55				N/A	7.18	
$La_{0.5}Sr_{0.5}FeO_3$					N/A	N/A	3.44				N/A	1.65	
$La_{0.3}Sr_{0.7}FeO_3$					N/A	N/A	1.84				N/A	1.37	
$La_{0.1}Sr_{0.9}FeO_3$					N/A	N/A	1.59				N/A	1.11	
$SrFeO_3$					N/A	N/A	2.52				N/A	1.86	
$SrMnO_3$	1173	100	3.13	20	N/A	84	9.39	100	3.13	10	N/A	1.26	Riaz *et al.*[66]
$La_{0.25}Sr_{0.75}MnO_3$					N/A	84	10.79				N/A	2.47	
$La_{0.5}Sr_{0.5}MnO_3$					N/A	91	11.84				N/A	1.88	
$LaMnO_3$					N/A	84	5.45				N/A	0.99	
$LaFe_{0.8}Al_{0.2}O_3$	1173	50	0.30	2.5	85	99	3.40	50	0.30	2.5	79	N/A	Xia *et al.*[67]
$LaFe_{0.8}Ga_{0.2}O_3$					78	99	3.10				72	N/A	
$LaFeO_3$					58	97	2.70				62	N/A	
$LaFe_{0.8}Sc_{0.2}O_3$					48	96	2.00				57	N/A	
10 wt% $SrFeO_{3-\delta}$-CaO	1253	4	0.38	6.59	88	96	9.90	5	0.77	N/A	N/A	5.12	Yu *et al.*[68]
30 wt% $SrFeO_{3-\delta}$-CaO				7.9	64	90	9.60				N/A	4.23	
60 wt% $SrFeO_{3-\delta}$-CaO				16.6	44	100	15.30				N/A	6.34	
80 wt% $SrFeO_{3-\delta}$-CaO				34.4	39	96	27.30				N/A	10.19	
$SrFeO_{3-\delta}$				16.5	35	100					N/A	3.71	
S–$La_{0.9}Sr_{0.1}FeO_3$/YSZ	1123	5	0.20	30	85–88	N/A	10.00	5	0.20	30	N/A	5.00	Sastre *et al.*[69]
M-$La_{0.9}Sr_{0.1}FeO_3$/YSZ					72	N/A	11.50				N/A	6.70	
$BaFe_2Al_{10}O_{19}$ (for 10 cycles)	1123	5	0.08	10	55–90	58–64	1.92–3.76	5	0.08	20	6–20	N/A	Zhu *et al.*[70]
$BaFe_3Al_9O_{19}$ (for 10 cycles)					65–78	64–88	2.38–3.26				13–38	N/A	
$BaFe_2MnAl_9O_{19}$ (for 10 cycles)					55–60	59–85	1.69–2.72				10–30	N/A	
$BaFe_2NiAl_9O_{19}$ (for 10 cycles)					100	55–70	3.16–4.21				22–56	N/A	
$BaFe_2CoAl_9O_{19}$ (for 10 cycles)					81–97	68–80	2.77–4.26				27–52	N/A	
$LaFe_3Al_9O_{19}$ (for 50 cycles)	1123	5	0.08	10	55–82	75–90	1.89–3.44	5	0.08	16	N/A	N/A	Zhu *et al.*[71]
Fe_2O_3–Al_2O_3 (for 10 cycles)					33–53	33–85	0.65–2.16				N/A	N/A	

Table 3 (*Contd.*)

OCs	Reduction step								Oxidation step					Reference
	Temperature/ K	CH_4 concentration/ %	Space velocity/ L min^{-1} g^{-1}	t/min	CH_4 conversion/ %	Syngas or CO selectivity/ %	Syngas yield/ mmol g^{-1}		CO_2 concentration/ %	Space velocity/ L min^{-1} g^{-1}	t/min	CO_2 conversion/ %	CO yield/ mmol g^{-1}	
$CeO_2/BaFe_3Al_9O_{19}$-700 (for 10 cycles)	1173	5	0.05	7	77–80	49–75	1.09–1.78		5	0.07	10	N/A	N/A	Cheng *et al.*[72]
$CeO_2/BaFe_3Al_9O_{19}$-800 (for 10 cycles)					77–84	49–75	1.11–1.72					N/A	N/A	
$CeO_2/BaFe_3Al_9O_{19}$-900 (for 10 cycles)					85–90	56–75	1.29–2.02					N/A	N/A	
$CeO_2/BaFe_3Al_9O_{19}$-1000 (for 10 cycles)					81–88	52–73	1.23–1.86					N/A	N/A	

structural optimization and support material integration, is essential for enhancing performance and stability as shown in Fig. 7. This technology offers a sustainable pathway for CO_2 utilization, aligning with global decarbonization goals.

3. Dry reforming of methane chemical looping (DRM-CL)

Given the ample and recoverable global reserves of natural and shale gas, DRM-CL, substituting CH_4 for H_2 in RWGS-CL, has emerged as a novel technology for co-producing syngas in reduction steps and CO in oxidation steps using two greenhouse gases. In comparison to conventional DRM, DRM-CL offers notable benefits: First, the carbon deposited in the reduction can be eliminated *via* reverse eqn (6) in the oxidation step by CO_2 with additional CO produced. Secondly, the side reaction of RWGS is avoided because the H_2 produced in the reduction step lacks contact with CO_2. Furthermore, unlike the strong oxidation of oxygen, the milder oxidant CO_2 facilitates the controlled oxidation of OCs with various valences (*i.e.* Fe species), which reportedly enables the selective CH_4 conversion to syngas.[61,62] Recent advancements in the introduction of concentrated solar power to supply the heat required for the endothermic reactions (*i.e.* DRM-CL, RWGS-CL) allow these processes to be operated with low carbon emissions and with sustainable, renewable properties.[63] Consequently, DRM-CL is acknowledged as a promising approach for producing high-quality, efficient, and cost-effective syngas. However, because of the existence of the side reactions of total oxidation of methane (TOM; eqn (10)) and carbon deposition (eqn (11)) in the reduction step, it still entails challenges in developing OCs with high selectivity to syngas, efficient regeneration through CO_2, marked oxygen storage capacity, effective mobility of lattice oxygen, and stable redox properties. During the last decade, remarkable progress has been made in developing various OCs for DRM-CL. The discussion presented hereinafter specifically examines representative OCs to establish a comprehensive structure–activity relation, offering valuable insights into the design rationale of future OCs.

Total oxidation of methane:

$$CH_4 + MO_x \rightarrow CO_2 + H_2O + MO_{x-\delta} \tag{10}$$

Methane pyrolysis:

$$CH_4\ (+\ M) \rightarrow 2H_2 + C_{(s)}\ (+\ M) \tag{11}$$

3.1 Composite oxides

Composite oxides such as perovskites and hexaaluminate materials are also investigated widely for DRM-CL. Table 3 presents a summary of the redox performance of composite OCs used in reviewed reports about DRM-CL.

3.1.1 Perovskites (ABO_3). Perovskite oxides (ABO_3) have received extensive attention in DRM-CL because of their flexibility to alter the composition, their high oxygen mobility rate, and their more or less high structural stability. The redox

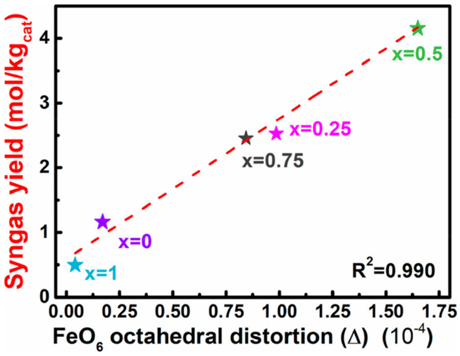

Fig. 8 Linear relation between the syngas yield and the FeO_6 octahedral distortion in $La_{1-x}Ce_xFeO_3$. Reprinted with permission.[64] Copyright 2020 American Chemical Society.

properties of perovskites can be tailored by substituting or replacing the cations in sites A or B. Substituting a divalent atom (*e.g.*, Sr) for the regular trivalent A-site element can engender an increased valence charge on the B-site transition metal and can engender the potential formation of oxygen vacancies, prompting the redox performance. A few reports of relevant research have described the effects of changing the doping content in the A site in perovskites on the redox properties for DRM-CL. For instance, Zhang *et al.* manipulated the distortion in FeO_6 octahedra by substituting different contents of Ce^{3+} in $La_{1-x}Ce_xFeO_3$ (x = 0, 0.25, 0.5, 0.75, 1).[64] They discovered that the syngas yield is related linearly to the FeO_6 octahedral distortion, as presented in Fig. 8. The increased FeO_6 octahedral distortion not only enhanced the bulk oxygen mobility and CO selectivity by inhibiting carbon deposition; it also prompted surface reactivity. Consequently, $La_{0.5}Ce_{0.5}FeO_3$, with the highest FeO_6 distortion, exhibited outstanding syngas productivity. In another case, Sastre *et al.* investigated the influence of strontium contents on the DRM-CL performance of $La_{1-x}Sr_xFeO_3$ (LSF) perovskites.[65] The oxygen storage capacity of LSF was correlated positively with the introduction content of strontium when $x \leq 0.7$, which was attributed to the facile reduction of Fe^{4+} to Fe^{3+}. The oxygen storage capacity of LSF tended to be stable when $x > 0.9$. However, structural instabilities occurred during CH_4 reduction, with the formation of Brownmillerite $Sr_2Fe_2O_5$ and segregated $LaFeO_3$. In fact, LSF with $x \leq 0.3$ exhibited superior CH_4 reforming performance, which was attributable to the CH_4 decomposition enhanced with strontium content increasing. It is noteworthy that perovskite recovery occurred in CH_4–CO_2 cycles and that H_2/CO control and production stability can be improved by higher-frequency cycles. The resilience of LSF perovskites enabled reactivity recovery even without optimal operating conditions. As part of a similar effort, Riaz *et al.* investigated the redox behaviours of $La_xSr_{1-x}MnO_3$ (LSM) for both DRM-CL and steam reforming of methane CL, using H_2O as a reoxidation medium (SRM-CL).[66] Although greater structural decomposition in LSM perovskites occurred during DRM-CL than during SRM-CL, the DRM-CL process still showed higher fuel-production efficiencies because of the reduced carbon deposition through strontium carbonates formed only by the reoxidation medium of CO_2. The introduction of lanthanum with x = 0.5 can enhance syngas yields to a different degree compared to those from pure $SrMnO_3$ and $LaMnO_3$ perovskites. However, the introduction of lanthanum with $x > 0.5$ altered the redox dynamics from stoichiometric to nonstoichiometric, leading to an overall decrease in syngas yields. This decrease was attributed to the incorporation of the important role of La in inhibiting the structural breakdown in the reduction step and in facilitating the adoption of nonstoichiometric redox reaction pathways. Furthermore, although the structure of LSM disintegrated over the redox cycles which are particularly evident at high strontium concentrations, Mn species actively participated in the processes and their oxidation states were closely related to the content of La and reoxidation medium (CO_2 or H_2O). Moreover, populating the B site with transition metals that possess diverse redox capabilities can influence the charge balance through oxidation or the creation of oxygen vacancies, which directly influence the reactivity of perovskites. For instance, Xia *et al.* incorporated redox-inert cations of Al, Ga, Fe, and Sc into the B site of $LaFe_{0.8}M_{0.2}O_3$ and found that manipulation of the tilting degree of the FeO_6 octahedron and the Fe–O bond length can be achieved through the doping of cations with varying radii.[67] It is noteworthy that the influence of the former was found to be predominant, strongly affecting both the oxygen mobility and Fe–O bond covalency. These factors, in turn, exert a strong effect on the reactivity of lattice oxygen and the consequent DRM-CL performance (Fig. 9). The accumulated findings demonstrated that $LaFe_{0.8}Al_{0.2}O_3$ showed enhanced oxygen exchange kinetics, improved methane activation capacity, and provided superior surface reaction activity by reducing FeO_6 octahedral tilting through smaller B-site cation doping.

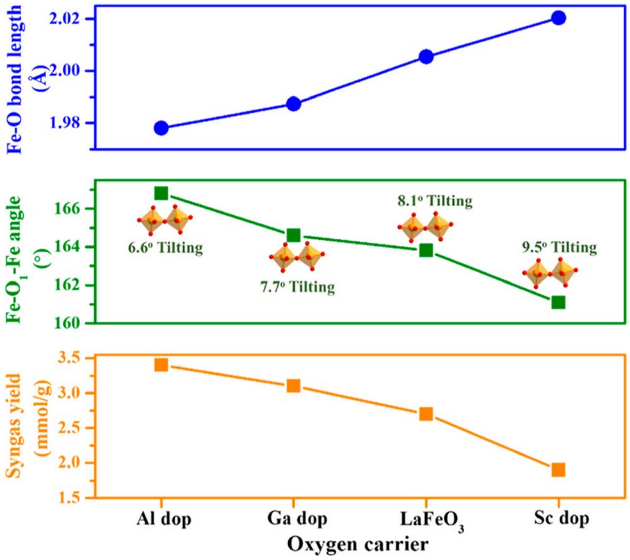

Fig. 9 Correlation between structural distortion and the CH_4 conversion performance in the first cycle over $LaFe_{0.8}M_{0.2}O_3$. Reprinted with permission.[67] Copyright 2022 American Chemical Society.

Furthermore, the redox performance of perovskites is reportedly improved by introducing additional potential components of matrix or supports. To overcome the challenges of $SrFeO_{3-\delta}$ perovskite posed by low stability and kinetics, Yu *et al.* encapsulated it within a CaO matrix and investigated the effects of the compositing perovskite weight percentage on the DRM-CL reactivity of x wt% $SrFeO_{3-\delta}$–CaO nanocomposites at 1253 K.[68] The 10 wt% $SrFeO_{3-\delta}$–CaO exhibited the highest syngas production rate and CH_4 conversion, whereas the 80 wt% $SrFeO_{3-\delta}$–CaO nanocomposite showed higher syngas productivity. A tradeoff was found between the quantity and speed of syngas production. The findings indicated that CaO primarily enhances the reduction of $SrFeO_{3-\delta}$ by methane and the stability for cycling. Additionally, it contributed oxygen species for the POM reaction, although to a limited extent. Furthermore, based on their earlier study demonstrating the remarkable DRM-CL activity of $La_{0.9}Sr_{0.1}FeO_3$ perovskite,[65] Sastre *et al.* dispersed it on yttria-stabilised zirconia (YSZ) with excellent oxygen transport capacity and high stability using two preparation methods of ball milling and perovskite synthesis.[69] Both samples prepared using different methods exhibited stable but unsatisfactory CO_2 and CH_4 conversion in the conventional DR process at 1123 K. However, $La_{0.9}Sr_{0.1}FeO_3$/YSZ exhibited better redox performance with high syngas production during DRM-CL. This better performance might be attributed to the improved CH_4 cracking and reverse Boudouard reactions. Moreover, despite its smaller surface area, the perovskite-synthesised composite exhibited better peak conversion in both CH_4 and CO_2 stages, along with enhanced H_2 production, possibly because of improved interaction among the components.

3.1.2 Hexaaluminates ($MAl_{12}O_{19}$). Hexaaluminates, with their unique layered structure and stability up to 1873 K, are excellent choices for high-temperature CH_4 conversion applications. Their structure, featuring alternating γ-Al_2O_3 spinel blocks and mirror planes with large cations (Ba, La, Sr), not only ensures exceptional sintering resistance; it also exhibits remarkable methane activation capabilities. Investigations of hexaaluminate composites include tailoring substitution by metal dopants and by introducing additional components. Zhu *et al.* prepared the Fe-substituted hexaaluminates, including $BaFe_2Al_{10}O_{19}$ and $BaFe_3Al_9O_{19}$, as well as bimetallic $BaFe_2MAl_9O_{19}$ (M = Mn, Ni, and Co) as OCs for DRM-CL and investigated the effects of Mn, Ni, and Co doping on the structure, reactivity, and stability.[70] Results indicated that the pure Fe-substituted OCs exhibited the coexistence of β-Al_2O_3 and magnetoplumbite (MP) hexaaluminate phases, transitioning from MP to β-Al_2O_3 during the CH_4/CO_2 redox process. In contrast, bimetallic $BaFe_2MAl_9O_{19}$ (M = Mn, Ni, and Co) crystallised exclusively in the β-Al_2O_3 hexaaluminate phase, retaining the β-Al_2O_3 structure even during CH_4 reduction. In actuality, Mn doping reduced the release of lattice oxygen, whereas Ni doping led to pronounced CH_4 pyrolysis. It is noteworthy that $BaFe_2CoAl_9O_{19}$ exhibited excellent reactivity and stability in CH_4/CO_2 redox cycles, with high CH_4 conversion and syngas yield as well as a desirable H_2/CO ratio around 2, which can be attributed to their enhanced oxygen-donation ability and the retention of the hexaaluminate phase across the DRM-CL redox cycles. Another case is that in which Zhu *et al.* investigated the feasibility of Fe-substituted La-hexaaluminate (LF3A) as an OC for the DRM-CL process.[71] Findings indicate that LF3A exhibited superior reactivity and stability over 50 cycles compared with conventional Fe–Al oxide (F3A, without La). The introduction of La led to the formation of the MP La-hexaaluminate structure, maintaining stability during deeper reduction for producing syngas. This introduction of La also enhanced the CH_4 reactivity toward syngas and the subsequent CO_2 usage. Within the MP La-hexaaluminate structure of LF3A, the distinct oxygen sites of O_6–Fe^{3+} (Oh) functioned mainly for total oxidation of methane (TOM), whereas O_5–Fe^{3+} (Tr) and O_4–Fe^{3+} (Th) played important roles in POM reaction. Moreover, the selective recovery of O_5–Fe^{3+} (Tr) and O_4–Fe^{3+} (Th) during CO_2 oxidation, as opposed to the regeneration of O_2 for O_6–Fe^{3+} (Oh), made CO_2 the preferred oxidant for improving synthesis gas selectivity. Because hexaaluminates have their own excellent stability, Cheng *et al.* used them as a support and loaded CeO_2 on $BaFe_3Al_9O_{19}$ (BF-3) hexaaluminate at different calcination temperatures (973–1273 K) to investigate the effects of CeO_2–hexaaluminate interaction on the DRM-CL redox performance.[72] Fresh CeO_2/BF-3 comprised CeO_2, β-Al_2O_3, and MP hexaaluminate. Elevating the calcination temperature from 973 K to 1173 K strengthened the interaction between CeO_2 and hexaaluminate, thereby facilitating the diffusion of lattice oxygen to the surface. However, 1273 K calcination induced sintering of the oxygen carrier, thereby impeding lattice oxygen migration. Among the various CeO_2/BF-3-T (T = 973–1273 K) configurations, CeO_2/BF3–1173 K emerged as a standout performer, exhibiting not only high CH_4 conversion (approx. 85%) and syngas yield (1.28–2.02 mmol g^{-1}) with an ideal H_2/CO ratio (approx. 2) but also exceptional CO_2 activation ability and stability during the redox cycles. The superior performance was attributed to the highest concentrations of Ce^{3+} and Fe^{2+}, abundant oxygen vacancies, and the formation of $CeFe_xAl_{1-x}O_3$.

3.2 Metal-based OCs

As a prerequisite, proper thermodynamic properties of OCs can be well illustrated by a modified Ellingham diagram, which portrays the change of standard Gibbs free energies of reactions (ΔG) with temperature (T). Modified Ellingham diagrams for OCs such as Fe-, Ce-, W-, Ni-, Cu-, and Co-based materials are presented as Fig. 10(a) and (b) for chemical looping combustion (CLC) using air instead of CO_2 for the oxidation step compared to DRM-CL; the one of supplemented and modified V-based oxides for DRM-CL is presented in Fig. 10(c).[73,74] In Fig. 10(b) and (c), materials in the combustion zone possess strong oxidising properties, suitable for CLC. In Fig. 10(b), the OCs only proceeded by a partial oxidation reaction are shown in the syngas production zone, which is also included as part of the partial oxidation zone for DRM-CL in Fig. 10(c) because of the unique ability of DRM-CL to mitigate carbon deposition through oxidation steps. Materials in the inert zone are inert and unsuitable as OCs. Moreover, the Gibbs free energy lines lower than that of CO_2 can proceed in CO_2 oxidation. Therefore,

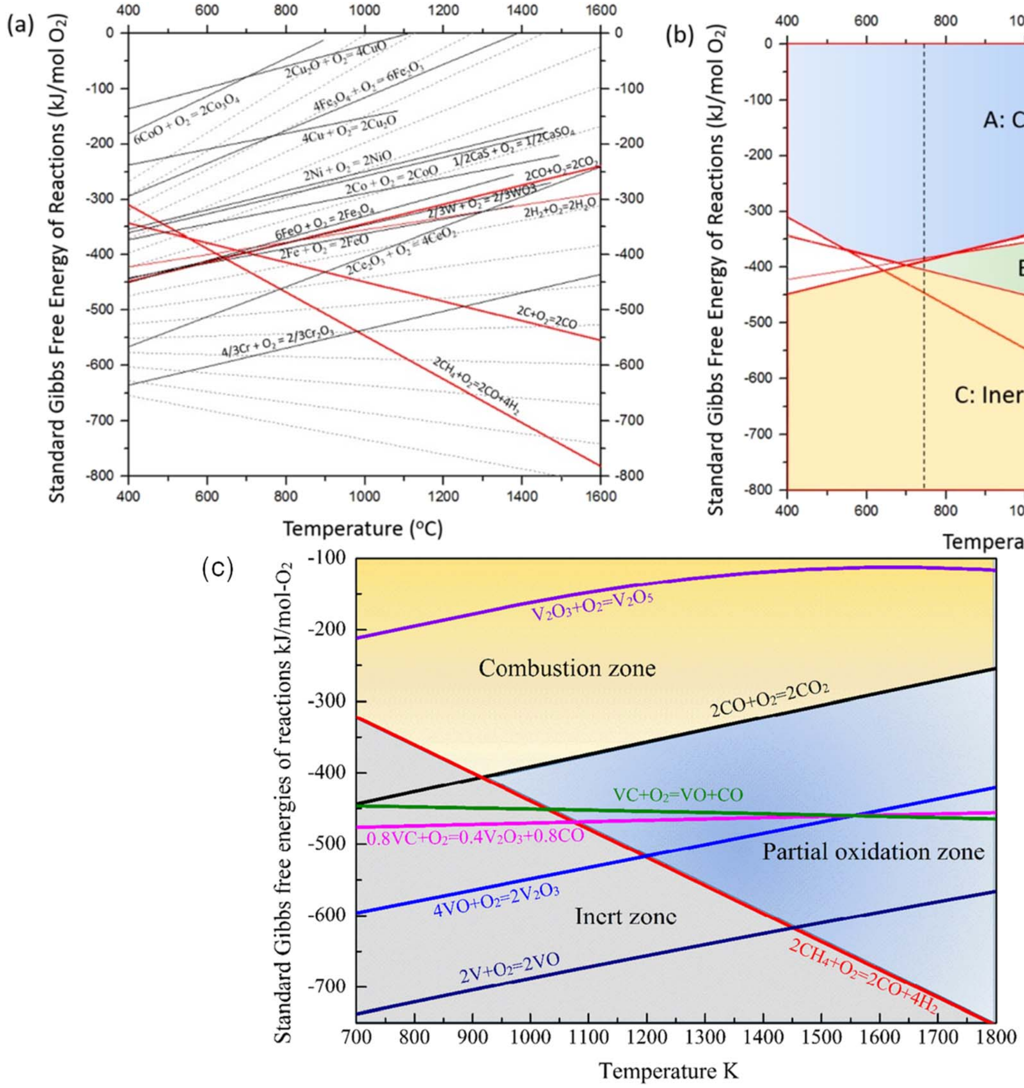

Fig. 10 Modified Ellingham diagrams for (a) standard Gibbs free energy changes of oxidation reactions of some OCs and (b) reaction zone division for CLC and syngas production applications. Reprinted with permission.[73] Copyright 2014 John Wiley and Sons. (c) V_2O_3-related species for DRM-CL. Reprinted with permission.[74] Copyright 2019 John Wiley and Sons.

according to Fig. 10(a), the lines of NiO, CoO, and CuO intersect within the combustion zone but are higher than the line of CO_2, indicating thermodynamic infeasibility in the CO_2 reoxidation step. The WO_3 line, which lies on the boundary between the combustion and partial oxidation zone, is lower than the CO_2 line, representing the potential for both partial oxidation and CO_2 oxidation. The Fe_2O_3 line lies close to the boundary between the combustion and partial oxidation zone, suggesting that the transformation from Fe_2O_3 to Fe_3O_4 is inclined toward combustion, whereas FeO to Fe is inclined toward partial oxidation of CH_4 (also thermodynamic favourability in CO_2 oxidation). In fact, CeO_2, which is situated in the partial oxidation zone, stands out as a candidate for DRM-CL with high syngas selectivity. As shown in Fig. 10(c), the curve of the V_2O_3–VC pair crosses over the middle of the partial oxidation zone, illustrating its desirable thermodynamic potential for both partial oxidation reaction and CO_2 oxidation reaction. In summary, Ce-, Fe-, W-, and V-based oxides are thermodynamically feasible and potential OCs for DRM-CL and these OCs. A handful of studies of metal-based OCs for DRM-CL have been conducted using this as a prerequisite assumption. Table 4 presents a summary of the DRM-CL performances of metal-based OCs described in recent reports.

3.2.1 Fe-based OCs. Because of their natural abundance, good environmental compatibility, and high CO_2 reoxidation activity, Fe-based OCs have received particular attention. Unfortunately, pure iron oxides are adversely affected by particle agglomeration, carbon deposition, and low CH_4 reactivity towards syngas. To overcome the limitations imposed upon pure iron oxide OCs, research efforts have assigned particular emphasis to the introduction of additional components of metal dopants, matrices or supports and have highlighted the design of the particle structure. A study by Zhang *et al.* examined iron-containing mixed metal oxides as highly

Table 4 Summary of redox performance of metal-based OCs for DRM-CL

	Reduction step								Oxidation step				
OCs	Temperature/K	CH_4 concentration/%	Space velocity/L min^{-1} g^{-1}	*t*/min	CH_4 conversion/%	Syngas or CO selectivity/%	Syngas yield/mmol g^{-1}	CO_2 concentration/%	Space velocity/L min^{-1} g^{-1}	*t*/min	CO_2 conversion/%	CO yield/mmol g^{-1}	Reference
$Sr_3Fe_2O_7$–$Ca_{0.5}Mn_{0.5}O$ (for 30 cycles)	1173	10	0.21	14.5	N/A	>95	1.53–4.42	10	0.21	6	N/A	1.56–1.8	Zhang *et al.*[75]
$SrFeO_3$–CaO (for 30 cycles)	1253	10		15	59	90.0	4.63	10		10	98	2.17	
Fe_2O_3/Al_2O_3 (for 10 cycles)	1073	100	0.22	60	73–93	10–18	N/A	100	0.22	60	68–85	N/A	Tang *et al.*[76]
Ce–Fe_2O_3/Al_2O_3 (for 10 cycles)					77–86	10–13	N/A				73–76	N/A	
$La_{0.33}Ce_{0.67}$–Fe_2O_3/Al_2O_3 (for 10 cycles)					77–83	9–10	N/A				65–76	N/A	
$La_{0.67}Ce_{0.33}$–Fe_2O_3/Al_2O_3 (for 10 cycles)					81–90	8–9	N/A				75–80	N/A	
La–Fe_2O_3/Al_2O_3 (for 10 cycles)					82–92	9–10	N/A				76–81	N/A	
0.5 wt% Rh/$LaCeO_{3.5-x}$	923	10	0.05	2	90	90.0	0.50	2	0.05	N/A	100	N/A	Haribal *et al.*[82]
8.8 wt% Ni/CeO_2	973	5	0.50	1	80	29.0	N/A	5	0.50	1	80	N/A	Löfberg *et al.*[83]
0.1 wt% Ni/CeO_2	1173	5	0.08, 0.50 (kinetic regime)	8	100	100	3.41	5	0.08, 0.50 (kinetic regime)	8	100	N/A	Han *et al.*[84]
Co/CeO_2	873	5	0.50	1	11	N/A	N/A	5	0.50	1	14	N/A	Guerrero-Caballero *et al.*[86]
	923				26	−100	N/A				28	N/A	
	973				51	−100	N/A				53	N/A	
	1023				68	−100	N/A				71	N/A	
	1073				79	−100	N/A				84	N/A	
Ni-phyllosilicate@ $Ce_{0.8}$, $Fe_{0.2}O_{2-\delta}$ (for 30 cycles)	893	5	0.25	8	79	83.0	4.50	5	0.25	8	N/A	2.81	Wang *et al.*[87]
$Fe_{0.88}Ni_{0.12}$–CeO_2	1273	16.7	0.06	10	99	$\gtrsim$90%	N/A	16.7	0.06	10	90	N/A	More *et al.*[61]
Physical mixture of 88%Fe + 12%Ni	1173	16.7	1.20	20	>95%	~70%	N/A	37.5	1.20	11	N/A	N/A	More *et al.*[62]
V_2O_3	1123	45	0.07	25–35	80–85	>99.5	N/A	40	0.06	25–35	N/A	N/A	Ge *et al.*[74]
Ni/WO_3(10)/ZrO_2 (for 180 cycles)	1023	30	2.50	2	70	>97%	N/A	30	2.50	3	45	N/A	Miyazaki *et al.*[88]

effective agents for a hybrid solar–redox scheme with DRM-CL.[75] Unsupported $Sr_3Fe_2O_{7-\delta}$ exhibited exceptional DRM-CL activity at 1173 K, but it was hindered by deactivation over redox cycles. However, dispersing $Sr_3Fe_2O_{7-\delta}$ in a $Ca_{0.5}Mn_{0.5}O$ matrix not only improved the redox stability considerably; it also achieved 96% syngas selectivity in the reduction step and nearly 100% CO_2 conversion in the oxidation step at 1173–1253 K. Furthermore, the hybrid solar–redox scheme with DRM-CL achieved remarkable CO production rates and productivity, surpassing state-of-the-art solar-thermal CO_2-splitting schemes at lower temperatures. Process simulation results show marked reductions in fossil energy consumption and in CO_2 emissions along with higher acetic acid production than those achieved using the conventional coal-based scheme. Tang *et al.* found that co-doping of La–Ce in Fe_2O_3/Al_2O_3 oxygen carrier efficiently enhanced its resistance to aggregation and decreased the carbon deposition, increasing the stability over redox cycles and ensuring the CO_2 activation for lattice oxygen replenishment.[76] These findings can be attributed to synergistic effects of La–Ce because of the abundant oxygen defects enhanced by intimate contact among active phases ($LaFeO_3$, $CeFeO_3$, CeO_2, Fe oxides, and Fe_3C) and surface dispersion of active phases and oxygen defects enhanced by CeO_2. Furthermore, Sun *et al.* synthesised Fe_2O_3/MgO microspheres with a core–shell structure using a hydrothermal method tailored for direct use in fluidised beds for DRM-CL.[77] The superior stability for DRM-CL was attributed to the presence of magnesium in the surface layer, which hindered iron ion diffusion and thereby avoided iron enrichment on the particle surface.

3.2.2 Ce-based OCs. For DRM-CL, Ce-based materials are highly appealing because of their oxygen mobility and storage capacity. From a thermodynamic perspective, the oxidation of reduced ceria by CO_2 is favourable across a wide temperature range, from 298 K to temperatures higher than 1273 K.[78] Additionally, reduction from CeO_2 to Ce_6O_{11} has been observed by Otsuka *et al.*, occurring as low as 923 K, which is consistent with thermodynamic calculations.[79] However, challenges arise because of the slow kinetics at lower temperatures. For conventional DRM, a consensus prevails that the kinetically relevant step is the activation of the C–H bond in CH_4 in conventional DRM, which should also initiate the DRM-CL process.[18,80] Consequently, numerous studies have introduced active additives for promoting the C–H bond activation to overcome the shortcomings of single CeO_2 related to the low kinetics of CH_4 conversion. Noble metals possess high resistance to coke deposition, with notable stability and CH_4 activation despite high cost and limited availability.[81] Also, Haribal *et al.* modified CeO_2 by La with the Ce/La ratio of 1 and promoted by Rh (0.5 wt%) for DRM-CL involved in the hybrid redox process (Fig. 11(a)).[82] The resultant $Rh/LaCeO_{3.5-x}$ exhibited 90% CH_4 conversion with a suitable $H_2:CO$ ratio of 2 : 1 for methanol synthesis and 100% CO_2 conversion to CO below 973 K. This high conversion can be attributed to the enhanced low-temperature bulk redox properties by La and improved surface properties for CH_4 activation by Rh. Operation at lower temperatures enables the integration with industrial waste heat, allowing a considerable reduction in energy requirements and CO_2 emissions for acetic acid production. Non-noble metals, especially Ni, were also used widely in CeO_2-based OCs because of their low cost, ready availability, and high CH_4 activation ability despite their higher carbon deposition compared to the noble metals. Löfberg *et al.* investigated Ni/

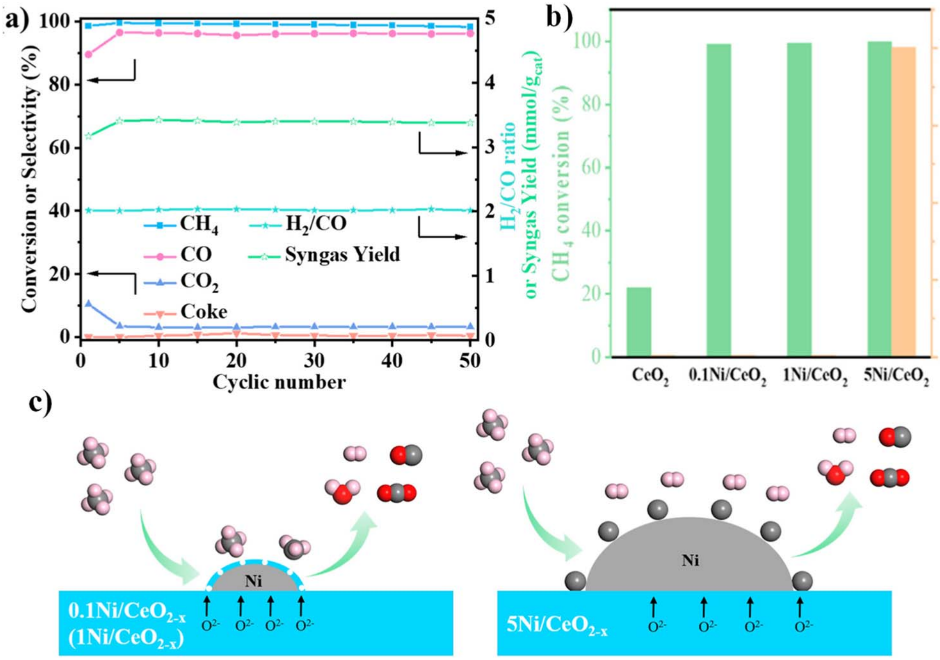

Fig. 11 (a) Performance over $0.1Ni/CeO_2$ in the partial oxidation of methane step during 50 cycles. (b) Comparison of CH_4 conversion and carbon deposition between CeO_2, $0.1Ni/CeO_2$, $1Ni/CeO_2$ and $5Ni/CeO_2$. (c) Proposed reaction pathways for the reduction step by CH_4 over $0.1Ni/CeO_2$ ($1Ni/CeO_2$) and $5Ni/CeO_2$. Reprinted with permission.[84] Copyright 2021 American Chemical Society.

CeO_2 with intermediate loading (approx. 8.8%).[83] It exhibited high selectivity toward H_2/CO without a high content of by-product H_2O produced. The deposited carbon was fully removed during the reoxidation step using CO_2. This removal was attributed to a synergistic effect at intermediate loadings of Ni, involving CH_4 activation facilitated by metallic Ni and enhanced oxygen mobility through the formation of a surface Ce–O–Ni solid solution. This effect is absent at low (2%) and high loadings (38%), for which insufficient active sites or surface solid solution species caused lower CH_4 conversion or coke formation. Moreover, Han *et al.* concentrated on the investigation of low loadings of Ni and found that loading of only 0.1 wt% or 1 wt% Ni on CeO_2 markedly enhanced the DRM-CL performance, with nearly 100% CH_4 conversion, CO selectivity, high syngas yields over 50 redox cycles, but without coke formation or reactivity degradation (Fig. 11(a)).[84] This superior performance is attributed to the encapsulation of Ni nanoparticles by CeO_2, preventing a considerable degree of Ni sintering during redox cycles and providing more oxygen vacancies for CH_4 activation (Fig. 11(c)). In contrast, 5 wt% Ni/CeO_2 exhibited severe carbon deposition because of the absence of encapsulation, leading to Ni nanoparticle sintering and CH_4 decomposition (Fig. 11(b) and (c)). Furthermore, Miyazaki *et al.* studied the redox properties of Ni/CeO_2, obtaining similar results showing low Ni loading reducing the coke deposition and effective enhancement of the DRM-CL performance.[85] However, immobilisation of other base metals (Fe, Co, Cu) did not enhance CO production. Apart from these efforts, they also investigated the redox properties of Ce species in 0.1 wt% Ni/CeO_2 using *operando* XANES and revealed that the DRM-CL process was accomplished by the reduction of Ce^{4+} to Ce^{3+} by CH_4 with syngas production followed by the subsequent reoxidation of Ce^{3+} to Ce^{4+} by CO_2, thereby confirming the crucially important role of CeO_2. Although a strong metal support interaction (SMSI) was observed in the previously described Ni/CeO_2 OCs, some potential exists for enhancing coking resistance because of Ni sintering and improving redox performance at lower temperatures. Strategies such as doping basic metal oxides and structurally tailoring the ceria support to anchor Ni nanoparticles have proven effective at reinforcing the SMSI effect, leading to improved coking resistance and lower operation temperatures.[86,87] Guerrero-Caballero *et al.* conducted a study of various ceria-based oxygen carriers based on the Ni/CeO_2, which is only active and selective at higher temperatures (>923 K).[86] Their findings indicate that Ni loading on homemade CeO_2 *via* impregnation and coprecipitation methods leads to similar redox performance, but that commercial CeO_2 is inactive. Actually, Zr doping enhanced the thermal stability of Ni/CeO_2 but adversely affected DRM-CL reactivity by enhancing the side reactions of methane total oxidation and carbon deposition. Notably, Co/CeO_2 exhibited promising performance, particularly at lower temperatures (873–923 K), providing a balance between surface activation and bulk oxygen species mobility. However, Fe/CeO_2 showed limited promise at 873–1073 K. Wang *et al.* combined the strategies of tailoring the structure and doping, and proposed sandwich and core–shell Ni-phyllosilicate@$Ce_{0.8}M_{0.2}O_{2-\delta}$ ($M = Fe, Co, Ni$) composites at lower temperatures (873–923 K).[87] These composites featured Ni-phyllosilicate cores and transition metal-doped CeO_2 shells, preventing over-sintering *via* an SMSI effect. As presented in Fig. 12, Ni nanoparticles were immobilised on spherical nuclei. The outermost doped CeO_2 shell acts as an oxygen donor. In fact, Ni-phyllosilicate@$Ce_{0.8}Fe_{0.2}O_{2-\delta}$ showed the best redox performance, with superior stability, oxygen storage capacity, and selectivity to syngas. *In situ* studies revealed that active intermediates (CH_X and deposited carbon) were formed on the surface and were then oxidised selectively by lattice oxygen toward syngas, with the formation of oxygen vacancies and Fe^0. These were subsequently re-oxidised to Ce^{4+} and Fe^{3+} during the CO_2 oxidation step.

3.2.3 Other metal-based OCs (V-based, W-based and Mo-based).

For DRM-CL, OCs based on metals such as V, W, and Mo have also been explored, aside from the extensively investigated Ce-based and Fe-based OCs described earlier. Ge *et al.* found

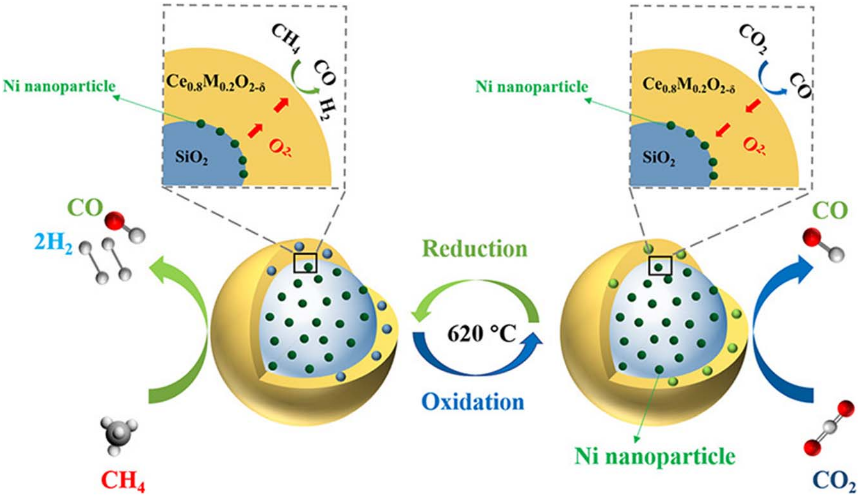

Fig. 12 Proposed reaction model for sandwich and core–shell Ni-phyllosilicate@$Ce_{0.8}M_{0.2}O_{2-\delta}$ ($M = Fe, Co, Ni$) composites. Reprinted with permission.[87] Copyright 2022 Elsevier.

that novel V_2O_3-based OC exhibited high syngas selectivity (>99.5%), CO_2 regeneration ability, and oxygen storage capacity because of the redox transformation between V_2O_3 and VC. Incorporating Pt–SiO_2 into pure V_2O_3 enhanced redox stability and kinetics.[74] The activation of C–H bonds, along with structural modification, was attributed to Pt–SiO_2–V_2O_3 interfaces, featuring coordinatively unsaturated Pt atoms and an oxygen-rich surface. The CH_4 reduction step (eqn (12)) involved a series of reactions, with VO serving as an intermediate connecting the reduction of V_2O_3 to VO (eqn (13)) and the subsequent transformation from VO to VC (eqn (14)). The introduction of Pt–SiO_2 boosted the kinetics of eqn (13) considerably, thereby influencing the rate-controlling step. After Miyazaki *et al.* investigated various WO_3-loaded materials with different loadings (6.2, 10.0, 19.5, and 30.0 wt%) and supports (ZrO_2 and Al_2O_3), they found Ni/WO_3(10)/ZrO_2 to be an ideal candidate OC for DRM-CL.[88] The results demonstrated that Ni-modified surface dispersed tungstate species on ZrO_2 were uniquely active as oxygen storage sites, with ZrO_2 and Ni contributing through reverse hydrogen spillover and hydrogen species recombination. The dispersed state in Ni/WO_3(10)/ZrO_2 was maintained during cycles; the DRM-CL process was achieved by the redox between W^{6+} and W^{0-3+}. Furthermore, Maeno *et al.* reported an effective Ni-modified MoO_3/ZrO_2 OC, which might work under isothermal conditions at 923 K.[89] They also showed an onset temperature of approximately 833 K in the CH_4-TPSR process. Optimal DRM-CL activity was achieved with 9.0 wt% MoO_3 loading because of the formation of predominantly two-dimensional molybdate species. The DRM-CL process was accomplished using a redox between Mo^{6+} and Mo^{4+}.

$$5CH_4 + V_2O_3 = 2VC + 3CO + 10H_2 \tag{12}$$

$$V_2O_3 + CH_4 = 2VO + CO + 2H_2 \tag{13}$$

$$VO + 2CH_4 = 2VC + CO + 4H_2 \tag{14}$$

3.2.4 Mixed metal-based OCs. Mixed metal-based OCs usually show enhanced performance by leveraging the advantages of the respective metal components. This smart combination of two metals gives broader potential for CL processes, allowing the reconciliation of contradictory demands in the coupled half-cycles. However, the stability of mixed metal-based OCs under the extreme conditions of high-temperature redox processes must be carefully considered because it might be a limiting factor in many cases, especially when compared with single-metal-based OCs. For instance, nickel oxides are often paired with iron oxides to harness the high reactivity of nickel for methane activation, complemented by the good selectivity of iron oxides for syngas formation. Additionally, the presence of iron contributes to the reduction of CO_2 to CO. More *et al.* reported that $Fe_{0.88}Ni_{0.12}$ alloy exhibited excellent performance for DRM-CL, achieving greater than 90% methane and CO_2 conversions at 1273 K.[61] The synergistic effects of Fe and Ni in the alloy enhanced methane reactivity. The presence of Fe enabled Ni oxidation with CO_2, a thermodynamically restricted process for pure Ni. This oxidation indicated strong metal coupling through oxygen transport in the solid carrier. The Fe_xNi_y carriers demonstrated stable operation without permanent dealloying within 50 cycles. As presented in Fig. 13, the CO selectivity and yield in the reduction step depend on the oxidation states of Fe during the reoxidation step, thereby highlighting the benefits of using a weak oxidant such as CO_2, which limited overoxidation thermodynamically and which allowed controlled oxidation state modulation because of slow kinetics. Later, their group found that such synergistic effects of Fe and Ni can be achieved even by physically mixing Fe_2O_3 and NiO.[62] In contrast to alloy carriers relying on the shared use of lattice oxygen, the DRM-CL process over the physical mixtures

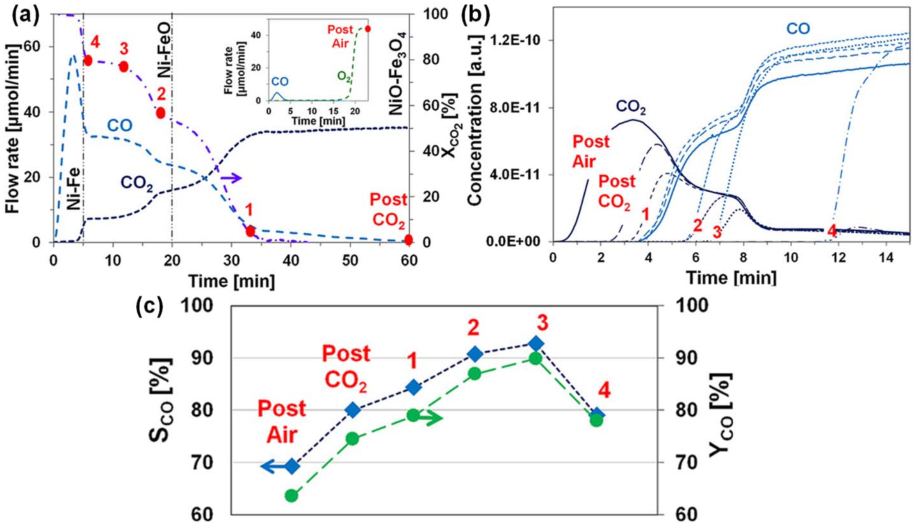

Fig. 13 (a) Reoxidation of $Fe_{0.88}Ni_{0.12}$–CeO_2 by CO_2 showing two regions of CO_2 conversion (>60% and <40%). (b) CO_2 and CO concentration profiles. (c) CO selectivity and yield. (All experiments were conducted after reduction by CH_4 at 1273 K. Red dots denote the time when the reoxidation was stopped. The inset in Fig. 12(a) shows reoxidation by O_2. Reduction half-cycles with CH_4 at 1273 K after different oxidation times, as indicated by the numbered spots.) Reprinted with permission.[61] Copyright 2019 John Wiley and Sons.

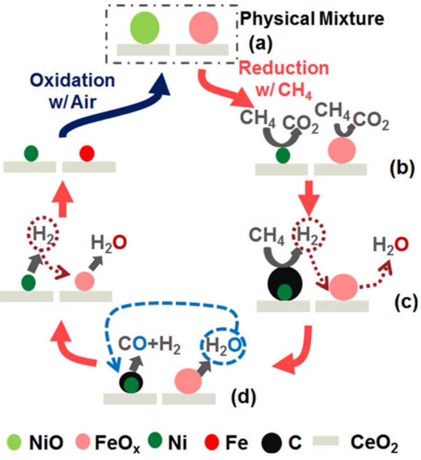

Fig. 14 Proposed reaction mechanism for Fe–Ni physical mixture. Reprinted with permission.[62] Copyright 2016 John Wiley and Sons.

of Ni and Fe was accomplished through the gas-phase mediated cooperative mechanism presented in Fig. 14.[61] Specifically, methane was cracked over Ni, forming carbon and H_2 (Fig. 14(c)). The intermediate H_2 was oxidised over Fe_xO_y with the production of steam, which subsequently gasified carbon on Ni, yielding final products CO and H_2 (Fig. 14(d)). This intricate process combined high methane activation rates over Ni with good syngas selectivity over Fe oxides, achieving near-complete methane conversion with syngas yields of approximately 70%. Expressed on a conceptual basis, H_2 acts as a gas-phase catalyst, catalysing iron oxide reduction and reforming from H_2O in carbon gasification. The process involved two nested catalytic cycles, constituting an intricate coupling for metal (oxide)-catalysed dry reforming reactions. Moreover, cerium oxides are paired with iron oxides because of their high oxygen storage capacity and excellent redox properties of cerium. A report by García-García *et al.* confirmed the increased syngas yields observed when using mixed oxides of iron and cerium instead of single-metal oxides.[90] These higher yields can be attributed to the synergetic interaction between Fe_2O_3 and CeO_2, the well dispersed Fe_2O_3 on CeO_2 support and the formation of perovskite structure (*i.e.* $CeFeO_3$). As concluded from Fig. 15, through precise manipulation of the Fe_2O_3/CeO_2 mass ratio, the initial oxidation state and reaction duration, the performance of the mixed oxides can be finely tuned to promote the oxidation of methane towards syngas. Simultaneously, this approach helped discourage the side reactions of both the complete oxidation of methane and coke formation.

3.3 Summary and prospects for DR-CL

DRM-CL is an innovative process using CH_4 and CO_2 to co-produce syngas and CO, offering advantages over conventional DRM, including carbon removal and selective CH_4 conversion. Challenges remain in developing oxygen carriers (OCs) with high syngas selectivity, efficient CO_2 conversion, and stable redox properties as shown in Fig. 16.

Perovskites and hexaaluminates are promising OCs thanks to their redox properties and structural stability. Tailored doping, such as Sr or Ce in perovskites, improves oxygen mobility and syngas yields. Hexaaluminates, particularly metal-doped variants, exhibit superior CH_4 reactivity and stability. Mixed and modified metal oxides (*e.g.*, Fe, Ce, V-based) optimise syngas production, highlighting future potential.

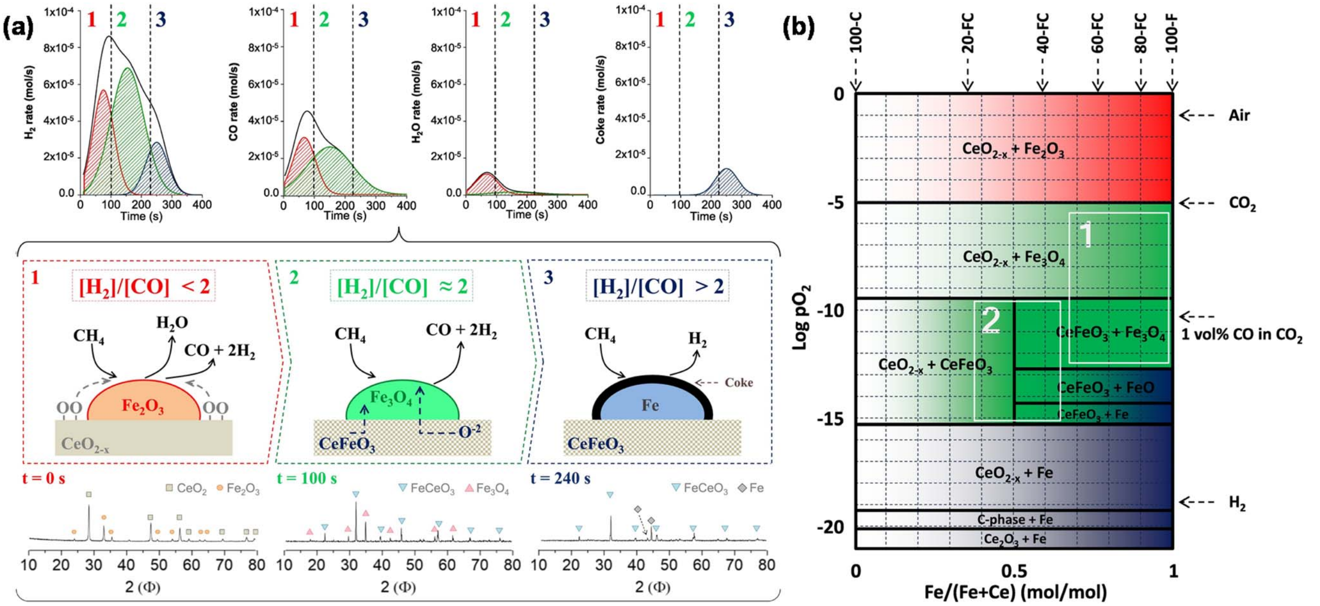

Fig. 15 (a) This schematic diagram portrays the evolution and correlation between the product selectivity of 40-FC with its oxidation state during the reduction step of the CLR process, following activation in carbon dioxide (*i.e.*, 90 min using 1.5 L min^{-1} (STP)). (b) Iron–cerium phase diagram to outline the phases and product selectivity to be anticipated during the reduction step of the CRM process at equilibrium for various combinations of iron–cerium contents and oxygen chemical potential at $T = 1173$ K and $P = 1$ atm. Reprinted with permission.[90] Copyright 2021 Elsevier.

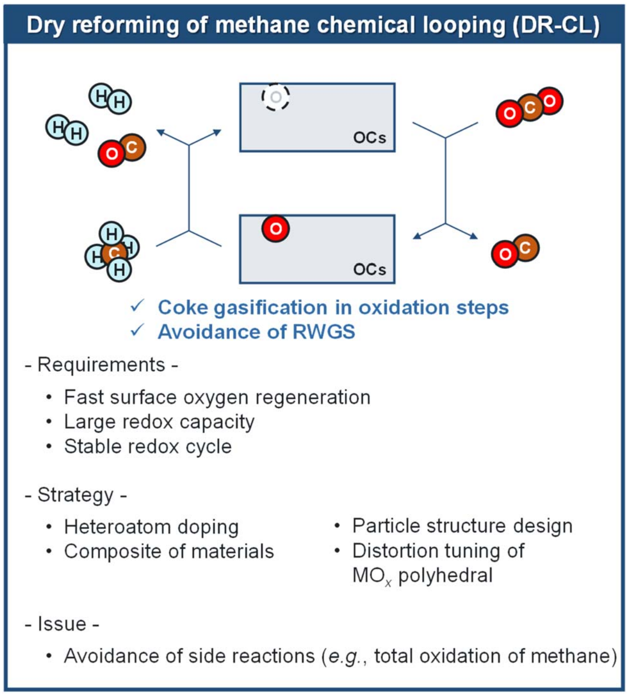

Dry reforming of methane chemical looping (DR-CL)

✓ Coke gasification in oxidation steps
✓ Avoidance of RWGS

\- Requirements -
- Fast surface oxygen regeneration
- Large redox capacity
- Stable redox cycle

\- Strategy -
- Heteroatom doping
- Composite of materials
- Particle structure design
- Distortion tuning of MO_x polyhedral

\- Issue -
- Avoidance of side reactions (*e.g.*, total oxidation of methane)

Fig. 16 Overview of material development for DR-CL.

4. Thermodynamic principles for screening oxygen carriers

The design of active OCs for CL processes necessitates the use of properties that ensure durability and sustained chemical reactivity through multiple redox cycles. To meet those cyclic behaviour requirements, specific characteristics must be incorporated into the OCs. Different chemical looping applications, such as DRM-CL and RWGS-CL, require distinct oxygen carrier properties to control product selectivity by addressing side reactions such as total oxidation of methane (TOM), carbon deposition for DRM-CL, and reduced conversion caused by reverse reactions in the oxidation step for RWGS-CL. Thermodynamic properties are regarded as prerequisites because they indicate the suitability of oxygen carriers for specific reactions and product selectivity. The following section presents an examination of the thermodynamic principles guiding the selection of active metal oxides for RWGS-CL and DRM-CL. The Ellingham diagram, a widely adopted tool in metallurgic studies, is useful for assessing the relative reduction potential of metal oxides at different temperatures.[91,92] It can be adapted further to evaluate the thermodynamic performance of metal oxides as OCs in various CL processes.[93]

In Fig. 18–22, we present modified Ellingham diagrams tailored for the effective classification and screening of oxygen carriers in the context of DRM-CL and RWGS-CL. Calculation details have been added to ESI† (text and Tables in Appendix). Here, 1 mol of O_2 was used as a virtual consumed oxygen species and a reaction intermediate. The overall Gibbs energy change (ΔG) of gas–solid reactions is calculable by subtracting ΔG of solid reactions with O_2 from those of reactant gas reactions with O_2, which engenders cancellation of O_2 in the reaction equations. This approach eases the assessment of the thermodynamic properties of metal oxides as OCs for CL, enabling selection based on specific process requirements. For instance, ΔG for the overall reaction $2CH_4 + MO_x = MO_{x-\delta} + 2CO + 4H_2$ (ΔG_0) can be ascertained from ΔG of the reactions of $2CH_4 + O_2 = 2CO + 4H_2$ (ΔG_1) and $MO_{x-\delta} + O_2 = MO_x$ (ΔG_2), through the calculation equation of $\Delta G_0 = \Delta G_1 - \Delta G_2$. Therefore, the feasibility of the corresponding overall gas–solid reactions for CL processes can be assessed easily according to the relative positions of the reactant gas reaction line and the solid reaction line on the modified Ellingham diagrams. When the solid material reaction line is above the gas reactant reaction line, the corresponding gas–solid reaction can occur. It is notable that the region below the line representing $2CO + O_2 = 2CO_2$ signifies the occurrence of CO_2 splitting reactions, given that CO_2 splitting is the reverse reaction of $2CO + O_2 = 2CO_2$. Based on these principles, in Fig. 17, oxide materials can be classified into five zones (No CO_2 splitting, Isothermal RWGS-CL, Total oxidation of methane (TOM), Partial oxidation of methane (POM), and an Inert Zone) according to their redox capability outlined by the following four key reactions:

$$\text{Reaction line 1: } 2CO + O_2 = 2CO_2$$

$$\text{Reaction line 2: } 2H_2 + O_2 = 2H_2O$$

$$\text{Reaction line 3: } 1/2CH_4 + O_2 = 1/2CO_2 + H_2O$$

$$\text{Reaction line 4: } 2CH_4 + O_2 = 2CO + 4H_2$$

4.1. No CO_2 splitting zone

Metal oxides positioned above reaction line 1 exhibit reduction properties that are too weak to accomplish a CO_2 splitting reaction in the common oxidation steps for both DRM-CL and RWGS-CL, rendering them unsuitable as materials for these two processes.

4.2. RWGS-CL zone

Metal oxides in this region are located between reaction lines 1 and 2; they exhibit thermodynamic conditions suitable for isothermal RWGS-CL reaction.

4.3 TOM zone

Metal oxides in this region, situated above reaction lines 2 and 3 but below line 1, are suitable OCs for the total oxidation of methane in DRM-CL, encompassing region B. However, because of their strong oxidizing properties, they are unsuitable for the partial oxidation of methane, rendering them unsuitable for DRM-CL.

4.4 POM (DRM-CL) zone

Metal oxides in this region are located between reaction lines 3 and 4. They are able to work as OCs for POM because of their

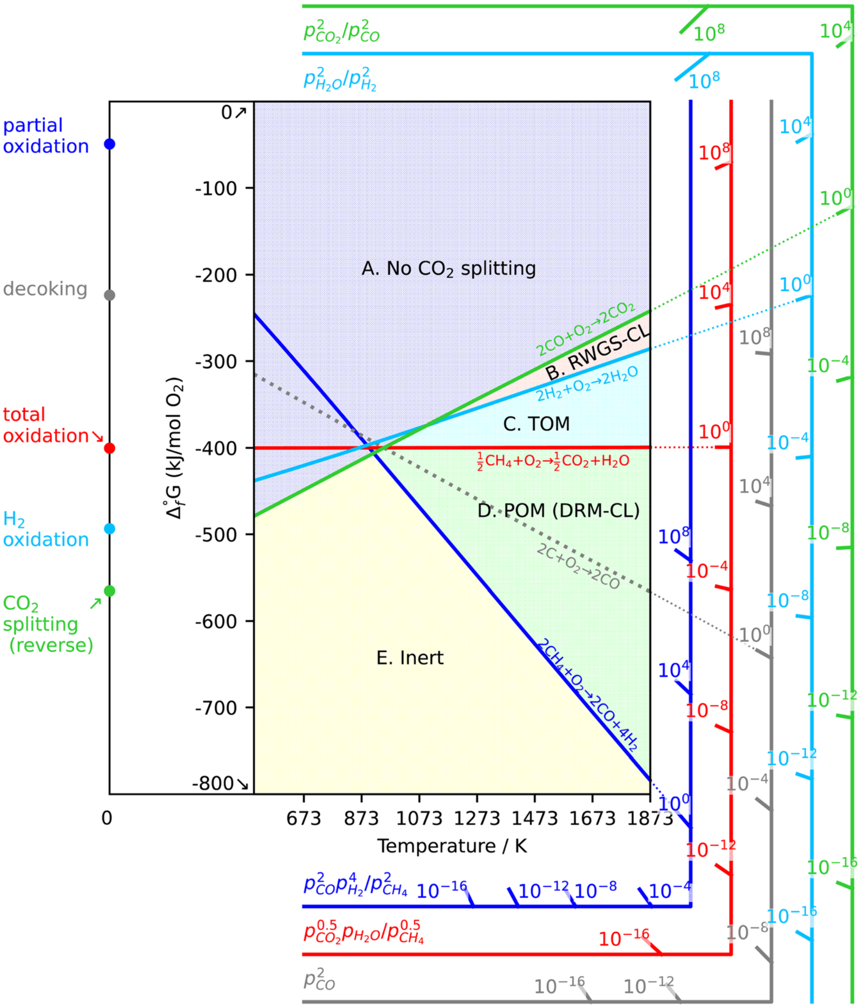

Fig. 17 Different zones for chemical looping processes. Reaction line 1: $2CO + O_2 = 2CO_2$. Reaction line 2: $2H_2 + O_2 = 2H_2O$. Reaction line 3: $1/2CH_4 + O_2 = 1/2CO_2 + H_2O$. Reaction line 4: $2CH_4 + O_2 = 2CO + 4H_2$.

moderate oxidising properties. These properties make them thermodynamically suitable for isothermal DRM-CL.

4.5 Inert zone

Metal oxides in this zone below line 4 lack the requisite oxidising properties to function as oxygen carriers. They are classified as inert materials for both RWGS-CL and DRM-CL.

The classification of metal oxides into specific zones underpins valuable insights into their suitability as OCs, not only for RWGS-CL and DRM-CL but also for other distinct CL processes that involve the outlined gas reaction lines (presented in Table 5). It is noteworthy that the dashed line corresponding to the reaction of $2C + O_2 = 2CO$ is indicative of the side reaction of carbon deposition in the reduction step of DRM-CL. Although it is not included in the classification zone because of the unique ability of DRM-CL to mitigate carbon deposition through oxidation steps, it plays an important role in guiding other relevant CL processes (*e.g.*, POM-CL, SRM-CL; in Table 5). Moreover, the reaction lines in the diagrams correspond to ΔG under atmospheric pressure conditions (partial pressure ratio of 1). The rationale behind the use of these classification zones in the figures is to screen materials under isothermal conditions. If non-isothermal conditions are applied to the oxidation and reduction steps, then more eligible materials might be available, but that discussion is not presented here. The partial pressure axes of the involved gas are also included to elucidate the effects of partial pressure on the thermodynamic properties of different metal oxides, which can be achieved by connecting the point at 0 K to the line representing the specific partial pressure ratio on the axis of the target reaction.

As shown in Fig. 18, several transition metal oxides (FeO_x, MnO_x, CeO_x, VO_x, PrO_x, CuO_x, CoO_x, NiO_x) and some common noble metal oxides (RhO_x, RuO_x, PdO_x, and PtO_x) with broad valence states and high oxygen capacity have been investigated as potential OCs. The comprehensive range of chemical redox reactions between different valence states for each metal oxide is considered. Some reaction lines of FeO_x and MnO_x are observed in the RWGS-CL region. Additionally, metal oxides such as FeO_x, MnO_x, CeO_x, VO_x, and PrO_x are apparent within the DRM-CL region. It is important to highlight that metal oxides such as FeO_x and MnO_x with multiple valence states require precise valence control to achieve optimal activity and

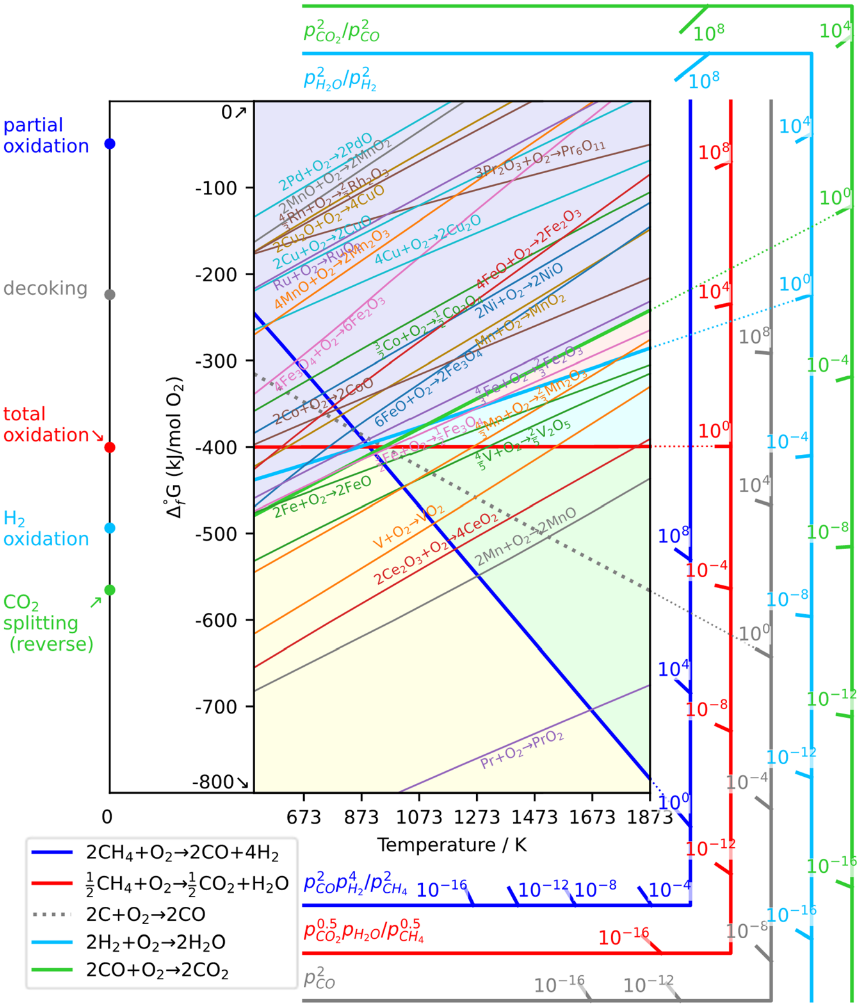

Fig. 18 Modified Ellingham diagram for single metal oxides as oxygen carriers for chemical looping.

selectivity from the thermodynamic results. Remarkably, the reaction lines of various valence states of CuO_x, CoO_x, NiO_x, RhO_x, RuO_x, PdO_x, and PtO_x are all located in the no CO_2 splitting zone, indicating them as unsuitable OCs for CO_2-splitting-related CL processes such as DRM-CL and RWGS-CL. The reaction line of PtO_x does not appear in the figure because $\Delta G > 0$ is within the investigated temperature range.

Single-metal oxide OCs have limited selectivity and reactivity. Introducing additional components has proved to be effective in enhancing their selectivity and reactivity. Metal oxides located in the no CO_2 splitting zone are regarded as promising additives for single-metal oxide OCs because of their distinctive thermodynamic properties preventing oxidation by CO_2, allowing them to remain as metal and form alloys with some OCs during the redox cycle. Alloys of these kinds involved in OCs have been widely reported for RWGS-CL and DRM-CL.[54,61,62] Herein, the thermodynamic results of potential alloys formed by the secondary metal oxides in no CO_2 splitting zone in Fig. 16 and metal oxides with multiple valence states such as FeO_x and MnO_x are presented in Fig. 19, with the filtered results displayed in Fig. 20. Figures showing Fig. 19 divided by metal combination to avoid line densification is shown in Fig. S1–S14.† Gibbs energies at representative temperatures in Fig. 19 are summarized in Tables S3 and S4.† It is readily apparent that most are distributed in the RWGS-CL and DRM-CL zone, underscoring the crucially important role of alloy formation for altering the thermodynamic properties of single metal OCs. Moreover, the application of some metal oxides such as Ga_2O_3 and In_2O_3 as OCs is restricted by the low melting point of their corresponding metals. According to findings from our earlier research,[58–60] forming alloys with a proper secondary metal from no CO_2 splitting zone in Fig. 18 was proved to increase their melting points effectively, thereby allowing the application of low-melting-point metals in RWGS-CL and DRM-CL. Based on these findings, various Ga-related and In-related alloy reaction lines were calculated. They are presented in Fig. 21 with the filtered results displayed in Fig. 22. Figures showing Fig. 21 divided by metal combination to avoid line densification is shown in Fig. S15–S28.† Gibbs energies at representative temperatures in Fig. 21 are listed in Tables S5 and S6.† Many of these alloys are found in both the RWGS-CL and DRM-CL zones, illustrating the high potential of applying the Ga-based and In-based alloy OCs in CL.

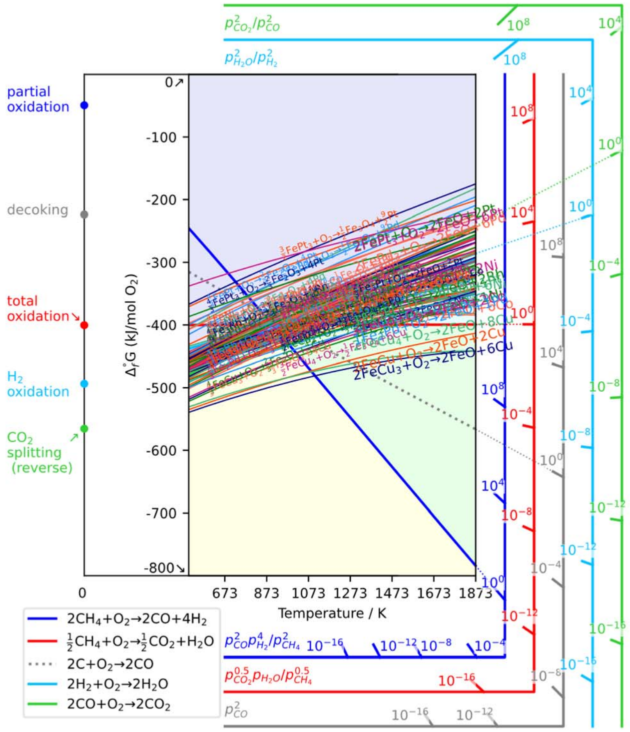

Fig. 19 Modified Ellingham diagram for all possible Fe-based or Mn-based alloy oxygen carriers during chemical looping.

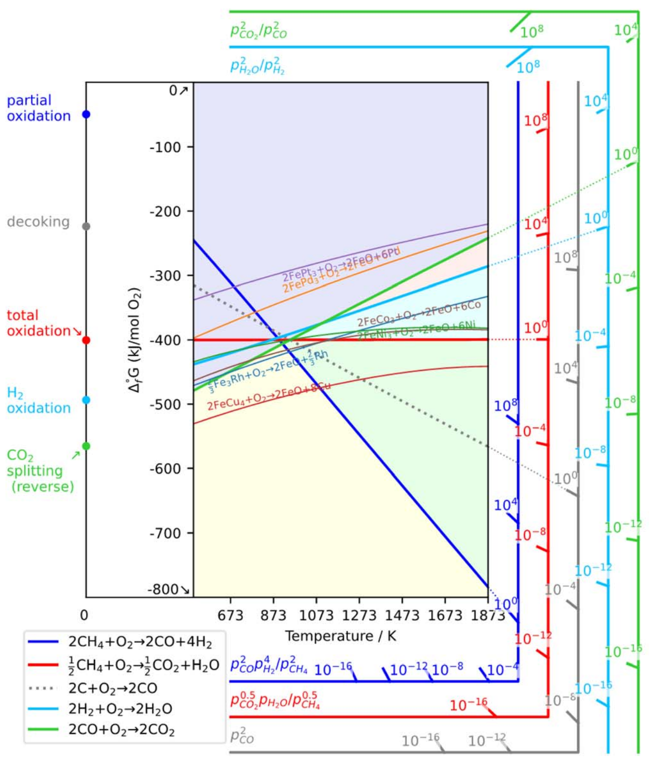

Fig. 20 Modified Ellingham diagram for oxygen carriers involving Fe- (left) or Mn- (right) based alloy formation during chemical looping.

Combining quantitative secondary components with single-metal oxides to form composites with specific structures and properties is another important strategy for improving the performance of single-metal-based OCs in RWGS-CL and DRM-CL. Based on the performance summaries in Tables 2 and 3, the La-based and Sr-based components are regarded as promising

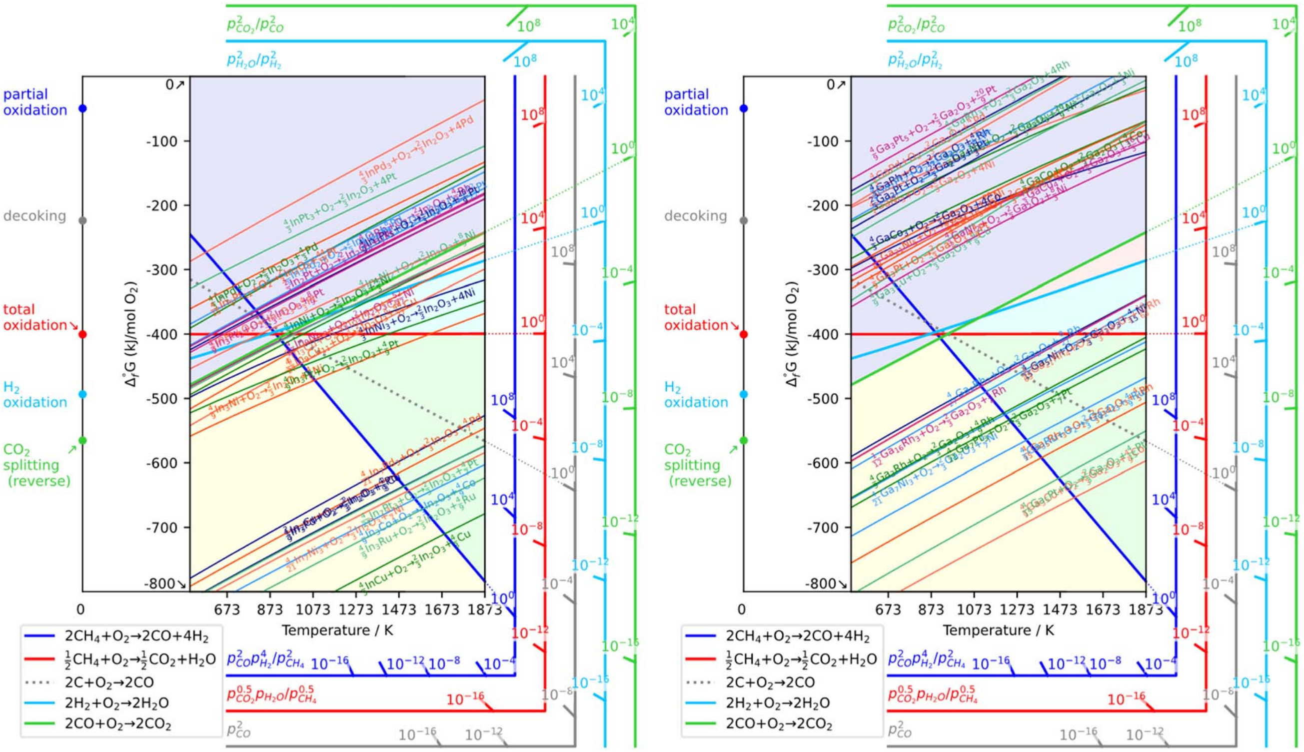

Fig. 21 Modified Ellingham diagram for all possible In-based or Ga-based alloy oxygen carriers during chemical looping.

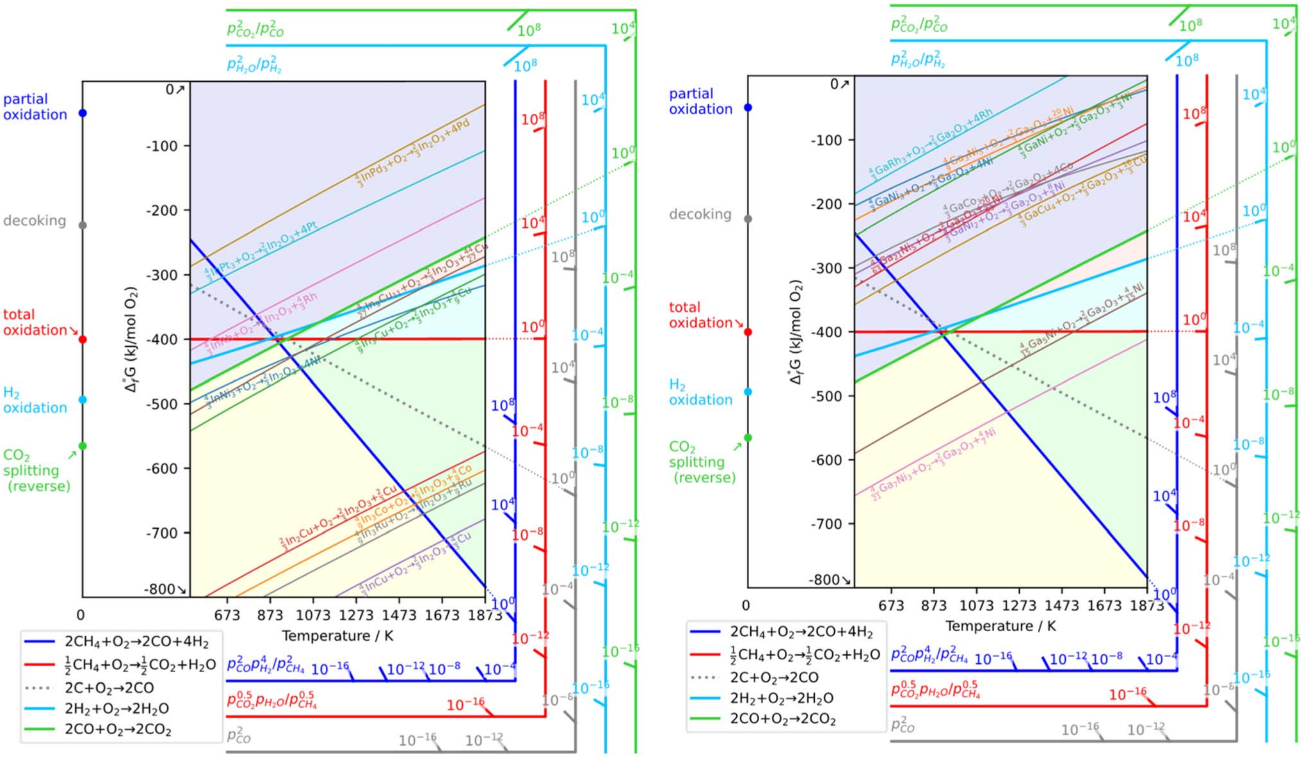

Fig. 22 Modified Ellingham diagram for oxygen carriers involving In- (left) or Ga- (right) based alloy formation during chemical looping.

Table 5 Chemical looping processes that involve the outlined gas reaction lines

Process name	Feedstock	Products	Product generation	Balance of the loop
RWGS-CL	CO_2	CO	**$MO_{x-1} + CO_2 \rightarrow MO_x + CO$**	**$MO_x + H_2 \rightarrow MO_{x-1} + H_2O$**
Thermochemical splitting	H_2O	H_2	**$MO_{x-1} + H_2O \rightarrow MO_x + H_2$**	$MO_x \rightarrow MO_{x-1} + 1/2O_2$
WGS-CL				**$MO_x + CO \rightarrow MO_{x-1} + CO_2$**
POM-CL	CH_4	Syngas	**$MO_x + CH_4 \rightarrow MO_{x-1} + CO + 2H_2$**	$MO_{x-1} + O_2 \leftrightarrow MO_x$
SRM-CL		Syngas, H_2		$MO_{x-1} + H_2O \leftrightarrow MO_x + H_2$
DRM-CL		Syngas, CO		$MO_{x-1} + CO_2 \leftrightarrow MO_x + CO$
Epoxidation-CL	C_{2+} hydrocarbon	Ethylene oxide	$C_2H_4 + MO_x \rightarrow MO_{x-1} + C_2H_4O$	**$MO_{x-1} + CO_2 \leftrightarrow MO_x + CO$**
ODH-CL		Ethylene	$C_2H_6 + MO_x \rightarrow MO_{x-1} + C_2H_4 + H_2O$	
ODH-CL		Propylene	$C_3H_8 + MO_x \rightarrow MO_{x-1} + C_3H_6 + H_2O$	
Selective oxidation-CL		Propionaldehyde	$1/2C_3H_8 + MO_x \rightarrow MO_{x-1} + 1/2C_3H_6O + 1/2H_2O$	
Selective oxidation-CL		Maleic anhydride	$1/7C_4H_{10} + MO_x \rightarrow MO_{x-1} + 1/7C_4H_2O_3 + 4H_2O$	
ODH-CL		Butadiene	$C_4H_8 + MeO_x \rightarrow MeO_{x-1} + C_4H_6 + H_2O$	
Oxidative cracking-CL		Ethylene	$C_6H_{14} + MeO_x \rightarrow MeO_{x-1} + 3C_2H_4 + H_2O$	

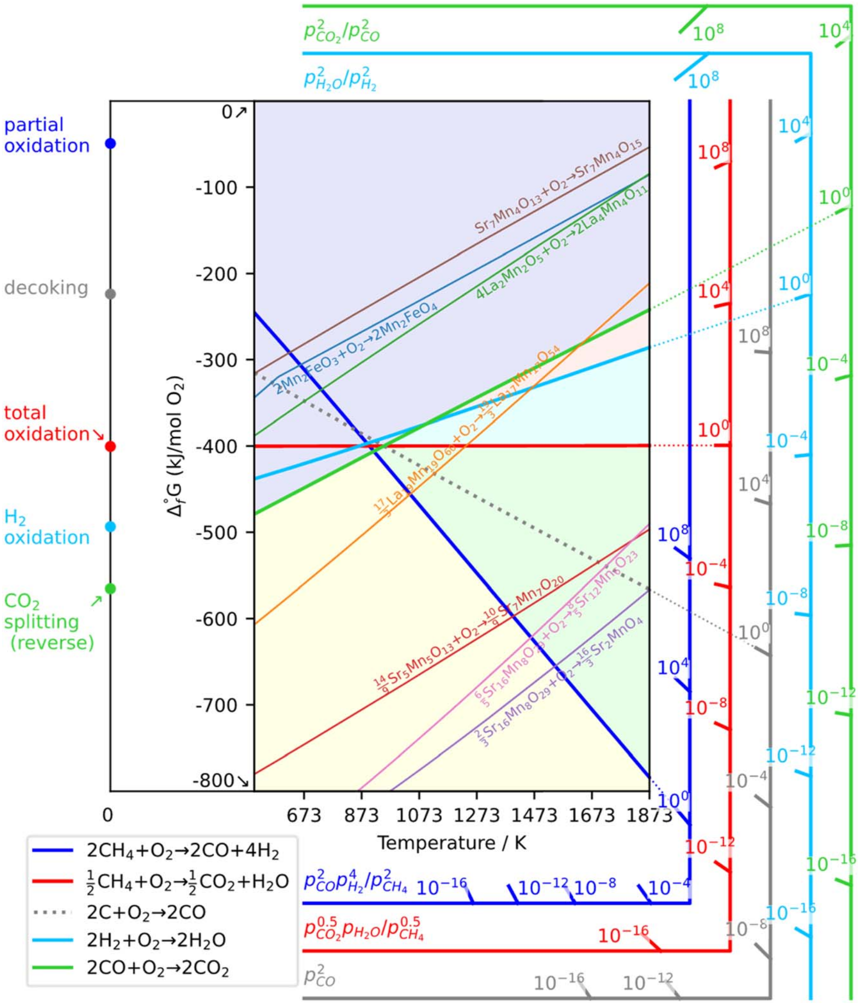

Fig. 23 Modified Ellingham diagram for composite oxides as oxygen carriers for chemical looping.

additives. Therefore, the thermodynamic results of some relevant example oxides are depicted in Fig. 23. The $La_xMn_yO_z$ demonstrate thermodynamic feasibility for both RWGS-CL and DRM-CL, whereas the $Sr_xMn_yO_z$ is thermodynamically feasible for DRM-CL.

5. Conclusion and future prospects

For CO_2 conversion, RWGS-CL and DRM-CL stand out as highly promising technologies, presenting versatile platforms for generating value-added chemicals efficiently with reduced pollutant emissions and using simplified product separation processes. Therefore, we have presented summaries of recent research on various OC developments in RWGS-CL and DRM-CL. Moreover, we introduced the thermodynamic principles for screening active OCs by proposing the modified Ellingham diagrams.

In the RWGS-CL process, H_2 facilitates the reduction of OCs, whereas CO_2 enables their regeneration. Achieving a balance between the strong reducing agent (H_2) and the weak oxidising agent (CO_2) is crucially important when screening OCs, allowing for lower isothermal operation temperatures in RWGS-CL. In fact, $La_{0.75}Sr_{0.25}FeO_{3-\delta}$ and $La_{1-x}Ba_xFeO_{3-\delta}$ emerge as superior OC candidates for RWGS-CL, showcasing exceptional CO_2 splitting performance even at temperatures as low as 823 K. To enhance their reactivity and stability, various approaches have been explored with specific examination of composition, particle size, porosity, structure, and specific surface area. Among metal-based OCs, Fe-based, In-based and Ga-based OCs all show promise because of their high oxygen capacity and outstanding CO_2 splitting performance. Generally, metal-based OCs exhibit higher oxygen capacity but are adversely affected by phase instability, whereas composite OCs offer better stability but lower oxygen capacity. Therefore, the synergistic combination of metal-based and composite OCs holds important potential, providing a balanced solution between oxygen capacity and stability.

With regard to DRM-CL, it proceeds by replacing H_2 with CH_4 in the reduction step. The selectivity of OCs toward partial oxidation of CH_4 for syngas generation is an important screening criterion for OCs. Moreover, although the replacement of commonly used air by CO_2 to regenerate OCs in the oxidation step presents opportunities to produce extra CO, it requires OCs to possess higher reactivity because of the weak oxidation ability of CO_2 compared to that of air. Composite OCs for DRM-CL demonstrate outstanding thermal stability and customisable redox properties through ion substitutional doping. To enhance the reactivity and redox stability of perovskites, manipulating the structural distortion of active sites by introducing different dopants or different contents of the same dopant can modify both bulk and surface properties. Additionally, incorporating supports and matrices can disperse segregated phases. Regarding hexaaluminates, choosing proper metal dopants and calcination temperatures can be attempted to retain the structure stability. Metal-based OCs, including Fe-, Ce-, V- and W-based OCs, have been examined extensively. Findings have revealed that Fe-based OCs are adversely affected by carbon deposition because the deeper reduction which facilitates the formation of CO engenders CH_4 decomposition on FeO sites. Introducing a support or matrix to control the particle size and designing a structure to encapsulate FeO represent efficient strategies to prevent carbon deposition. It is known that Ce-based OCs are adversely affected by inferior CH_4 conversion because of incomplete reduction of Ce^{4+} to Ce^{3+}. Introducing surface promoters such as Ni and doping CeO_2 with additives can lower the CH_4 activation energy and promote stoichiometric redox solid-phase reactions, respectively. Consequently, these materials can ensure the complete reduction of Ce^{4+} to Ce^{3+}, increasing the syngas yield. The V-based and W-based OCs, which are recently developed OCs for DRM-CL, have also shown great potential superior redox properties. They represent another promising research direction for future investigation.

Beyond the properties and performances of OCs detailed earlier, modified Ellingham diagrams that exhibit the thermodynamic properties of potential metal oxides for the effective screening of active OCs of DRM-CL and RWGS-CL were first proposed, offering valuable insights not only for RWGS-CL and DRM-CL but also for other distinct CL processes involve similar reactions.

Enhancing the redox performance of OCs at lower temperatures is crucially important for both RWGS-CL and DRM-CL. This enhancement involves an emphasis on improving the dispersion of metal nanoparticles, ensuring optimal exposure of active sites for efficient methane and CO_2 activation. Although the current understanding of "CO_2 to CO" CL technologies remains limited, remarkable progress is necessary for elucidating redox mechanisms, refining structure design, optimising reactor and process operations, and scaling up processes. By integrating synthetic chemistry, computational chemistry, and various *in situ* characterisation techniques such as spectroscopy, diffraction and microscopy, CL for the production of CO or syngas from CO_2 has emerged as a largely unexplored and exceptionally promising area of research with important potential applications.

The design of active oxygen carriers (OCs) for chemical looping (CL) processes requires durability and sustained reactivity across multiple redox cycles. Each CL process, such as reverse water gas shift (RWGS-CL) or dry reforming of methane (DRM-CL), necessitates specific OC properties to optimise product selectivity and mitigate side reactions, like carbon deposition or side reactions. Thermodynamic properties are essential for evaluating OCs, with tools like modified Ellingham diagrams aiding in classification and selection based on reaction feasibility. In these diagrams, the Gibbs energy change (ΔG) of gas–solid reactions is calculated by subtracting ΔG values of solid and gas reactions involving oxygen. This approach enables easy assessment of whether a reaction can occur, depending on the relative positions of reaction lines. Materials are classified into several zones (*e.g.*, RWGS-CL, DRM-CL, no CO_2 splitting) based on redox capability, guiding their suitability for specific CL processes. FeO_x and MnO_x show promise in RWGS-CL and DRM-CL, though their multiple valence states require precise control for optimal performance. Single-metal OCs often have limited selectivity and reactivity, but alloy formation with secondary metals enhances these properties. Metal oxides from the no CO_2 splitting zone, when alloyed with others like FeOx and MnO_x, can improve melting points and expand applicability. For example, Ga- and In-based alloys have been shown to increase melting points and demonstrate potential in RWGS-CL and DRM-CL. Further optimisation using various methods, including informatics or machine learning,[94] also helps us to obtain better materials. The integration of thermodynamic principles with alloy design has advanced the development of versatile and efficient OCs for diverse CL processes.

Data availability

The data supporting this article have been included as part of the ESI.†

Conflicts of interest

There are no conflicts to declare.

Acknowledgements

A part of this work was supported by JST-ALCA-Next Program Grant Number 23836167, Japan; International Leading Research (grant no. 23K20034) from the Japan Society for the Promotion of Science, Japan; Project 22P51 at Waseda Research Institute for Science and Engineering; Cabinet Office grant in aid "Evolution to Society 5.0 Agriculture Driven by IoP (Internet of Plants)," Japan; and Grant-in-Aid for JSPS Fellows from the Japan Society for the Promotion of Science (JP24KJ2090).

References

1 S. J. Davis, K. Caldeira and H. D. Matthews, Future CO_2 Emissions and Climate Change from Existing Energy Infrastructure, *Science*, 2010, **329**, 1330–1333.

2 M. Aresta, A. Dibenedetto and A. Angelini, Catalysis for the Valorization of Exhaust Carbon: from CO_2 to Chemicals, Materials, and Fuels. Technological Use of CO_2, *Chem. Rev.*, 2014, **114**, 1709–1742.

3 S. Perathoner and G. Centi, CO_2 Recycling: A Key Strategy to Introduce Green Energy in the Chemical Production Chain, *ChemSusChem*, 2014, **7**, 1274–1282.

4 D. S. Mallapragada, N. R. Singh, V. Curteanu and R. Agrawal, Sun-to-Fuel Assessment of Routes for Fixing CO_2 as Liquid Fuel, *Ind. Eng. Chem. Res.*, 2013, **52**, 5136–5144.

5 J. Artz, T. E. Müller, K. Thenert, J. Kleinekorte, R. Meys, A. Sternberg, A. Bardow and W. Leitner, Sustainable Conversion of Carbon Dioxide: An Integrated Review of Catalysis and Life Cycle Assessment, *Chem. Rev.*, 2018, **118**, 434–504.

6 F. V. Vázquez, J. Koponen, V. Ruuskanen, C. Bajamundi, A. Kosonen, P. Simell, J. Ahola, C. Frilund, J. Elfving, M. Reinikainen, N. Heikkinen, J. Kauppinen and P. Piermartini, Power-to-X technology using renewable electricity and carbon dioxide from ambient air: SOLETAIR proof-of-concept and improved process concept, *J. CO2 Util.*, 2018, **28**, 235–246.

7 P. G. Loutzenhiser, M. E. Gálvez, I. Hischier, A. Stamatiou, A. Frei and A. Steinfeld, CO_2 Splitting *via* Two-Step Solar Thermochemical Cycles with Zn/ZnO and FeO/Fe_3O_4 Redox Reactions II: Kinetic Analysis, *Energy Fuels*, 2009, **23**, 2832–2839.

8 S. Fujimori and S. Inoue, Carbon Monoxide in Main-Group Chemistry, *J. Am. Chem. Soc.*, 2022, **144**(5), 2034–2050.

9 R. M. B. Carrilho, M. J. F. Calvete, G. Mikle, L. Kollár and M. M. Pereira, Carbon Monoxide as C1 Building Block in Fine Chemical Synthesis, *Chin. J. Chem.*, 2024, **42**, 199–221.

10 K. T. Rommens and M. Saeys, Molecular Views on Fischer-Tropsch Synthesis, *Chem. Rev.*, 2023, **123**(9), 5798–5858.

11 J. E. A. -Hernández, S. L. Bertoli, H. G. Riella, C. Soares and N. Padoin, An Overview of Low-Temperature Fischer–Tropsch Synthesis: Market Conditions, Raw Materials, Reactors, Scale-Up, Process Intensification, Mechanisms, and Outlook, *Energy Fuels*, 2024, **38**(1), 1–28.

12 D. S. Mallapragada, N. R. Singh, V. Curteanu and R. Agrawal, Sun-to-Fuel Assessment of Routes for Fixing CO_2 as Liquid Fuel, *Ind. Eng. Chem. Res.*, 2013, **52**, 5136–5144.

13 J. Benoit, D. Perry and K. Mondal, Fischer–Tropsch Synthesis in supercritical CO_2 – Inhibition of CO_2 selectivity for enhanced hydrocarbon production, *Fuel*, 2017, **209**, 383–393.

14 P. Furler, J. R. Scheffe and A. Steinfeld, Syngas production by simultaneous splitting of H_2O and CO_2 *via* ceria redox reactions in a high-temperature solar reactor, *Energy Environ. Sci.*, 2012, **5**, 6098–6103.

15 S. S. Ail and S. Dasappa, Biomass to liquid transportation fuel *via* Fischer–Tropsch synthesis – Technology review and current scenario, *Renew. Sustain. Energy Rev.*, 2016, **58**, 267–286.

16 X. Su, X. Yang, B. Zhao and Y. Huang, Designing of highly selective and high-temperature endurable RWGS heterogeneous catalysts: recent advances and the future directions, *J. Energy Chem.*, 2017, **26**, 854–867.

17 X. Chen, Y. Chen, C. Song, P. Ji, N. Wang, W. Wang and L. Cui, Recent Advances in Supported Metal Catalysts and Oxide Catalysts for the Reverse Water–Gas Shift Reaction, *Front. Chem.*, 2020, **8**, 709.

18 N. A. K. Aramouni, J. G. Touma, B. A. Tarboush, J. Zeaiter and M. N. Ahmad, Catalyst design for dry reforming of methane: analysis review, *Renew. Sustain. Energy Rev.*, 2018, **82**, 2570–2585.

19 C. Palmer, D. C. Upham, S. Smart, M. J. Gordon, H. Metiu and E. W. McFarland, Dry reforming of methane catalysed by molten metal alloys, *Nat. Catal.*, 2020, **3**, 83–89.

20 K. Wittich, M. Krämer, N. Bottke and S. A. Schunk, Catalytic Dry Reforming of Methane: Insights from Model Systems, *ChemCatChem*, 2020, **12**, 2130–2147.

21 X. Zhu, Q. Imtiaz, F. Donat, C. R. Müller and F. Li, Chemical looping beyond combustion – a perspective, *Energy Environ. Sci.*, 2020, **13**, 772–804.

22 H. J. Richter and K. F. Knoche, *Efficiency and Costing*, ed. R. A. Gaggioli, ACS Publications, Washington DC, 1983, ch. 3, vol. 235, pp. 71–85.

23 M. Tang, L. Xu and M. Fan, Progress in oxygen carrier development of methane-based chemical-looping reforming: A review, *Appl. Energy*, 2015, **151**, 143–156.

24 M. Tian, C. Wang, Y. Han and X. Wang, Recent Advances of Oxygen Carriers for Chemical Looping Reforming of Methane, *ChemCatChem*, 2021, **13**, 1615–1637.

25 M. Najera, R. Solunke, T. Gardner and G. Veser, Carbon capture and utilization *via* chemical looping dry reforming, *Chem. Eng. Res. Des.*, 2011, **89**, 1533–1543.

26 D. Li, R. Xu, Z. Gu, X. Zhu, S. Qing and K. Li, Chemical-Looping Conversion of Methane: A Review, *Energy Technol.*, 2019, **8**, 1900925.

27 L. Zeng, Z. Cheng, J. A. Fan, L. S. Fan and J. Gong, Metal oxide redox chemistry for chemical looping processes, *Nat. Rev. Chem*, 2018, **2**, 349–364.

28 M. M. Hossain and H. I. de Lasa, Chemical-looping combustion (CLC, for inherent CO_2 separations – a review, *Chem. Eng. Sci.*, 2008, **63**, 4433–4451.

29 J. Hu, V. V. Galvita, H. Poelman and G. B. Marin, Advanced Chemical Looping Materials for CO_2 utilization: A Review, *Materials*, 2018, **11**, 1187.

30 D. Song, Y. Lin, C. Li, S. Fang, F. He, Z. Huang, Z. Zhao, Y. Xiong and H. Huang, Review on Migration and Transformation of Lattice Oxygen during Chemical Looping Conversion: Advances and Perspectives, *Energy Fuels*, 2023, **37**, 5743–5756.

31 A. Lyngfelt, Chemical Looping Combustion: Status and Development Challenges, *Energy Fuels*, 2020, **34**(8), 9077–9093.

32 L. C. Buelens, H. Poelman, G. B. Marin and V. V. Galvita, *110th* Anniversary: Carbon Dioxide and Chemical Looping: Current Research Trends, *Ind. Eng. Chem. Res.*, 2019, **58**(36), 16235–16257.

33 B. J. Hare, D. Maiti, Y. A. Daza, V. R. Bhethanabotla and J. N. Kuhn, Enhanced CO_2 Conversion to CO by Silica-Supported Perovskite Oxides at Low Temperatures, *ACS Catal.*, 2018, **8**, 3021–3029.

34 V. V. Galvita, H. Poelman, V. Bliznuk, C. Detavernier and G. B. Marin, CeO_2-Modified Fe_2O_3 for CO_2 utilization *via* Chemical Looping, *Ind. Eng. Chem. Res.*, 2013, **52**, 8416–8426.

35 Y. A. Daza, R. A. Kent, M. M. Yung and J. N. Kuhn, Carbon dioxide conversion by reverse water–gas shift chemical looping on perovskite-type oxides, *Ind. Eng. Chem. Res.*, 2014, **53**, 5828–5837.

36 N. V. R. A. Dharanipragada, L. C. Buelens, H. Poelman, E. De Grave, V. V. Galvita and G. B. Marin, Mg-Fe-Al-O for advanced CO_2 to CO conversion: carbon monoxide yield *v.s.* oxygen storage capacity, *J. Mater. Chem. A*, 2015, **3**, 16251–16262.

37 A. E. Ramos, D. Maiti, Y. A. Daza, J. N. Kuhn and V. R. Bhethanabotla, Co, Fe, and Mn in La-perovskite oxides for low temperature thermochemical CO_2 conversion, *Catal. Today*, 2019, **338**, 52–59.

38 Y. A. Daza, D. Maiti, R. A. Kent, V. R. Bhethanabotla and J. N. Kuhn, Isothermal reverse water gas shift chemical looping on $La_{0.75}Sr_{0.25}Co_{(1-Y)}FeYO_3$ perovskite-type oxides, *Catal. Today*, 2015, **258**, 691–698.

39 J. E. ten Elshof, H. J. M. Bouwmeester and H. Verweij, Oxygen transport through $La_{1-x}Sr_xFeO_{3-\delta}$ membranes II. Permeation in air/CO, CO_2 gradients, *Solid State Ionics*, 1996, **89**, 81–92.

40 V. C. Corberán, L. G. Tejuca and A. T. Bell, Surface reactivity of reduced $LaFeO_3$ as studied by TPD and IR spectroscopies of CO, CO_2 and H_2, *J. Mater. Sci.*, 1989, **24**, 4437–4442.

41 H. Ullmann, N. Trofimenko, F. Tietz, D. Stöver and A. Ahmad-Khanlou, Correlation between thermal expansion and oxide ion transport in mixed conducting perovskite-type oxides for SOFC cathodes, *Solid State Ionics*, 2000, **138**, 79–90.

42 B. J. Hare, D. Maiti, S. Ramani, A. E. Ramos, V. R. Bhethanabotla and J. N. Kuhn, Thermochemical conversion of carbon dioxide by reverse water–gas shift chemical looping using supported perovskite oxides, *Catal. Today*, 2019, **323**, 225–232.

43 J. C. Brower, B. J. Hare, V. R. Bhethanabotla and J. N. Kuhn, Mesoporous Silica Supported Perovskite Oxides for Low Temperature Thermochemical CO_2 Conversion, *ChemCatChem*, 2020, **12**, 6317–6328.

44 A. Jo, Y. Kim, H. S. Lim, M. Lee, D. Kang and J. W. Lee, Controlled template removal from nanocast $La_{0.8}Sr_{0.2}FeO_3$ for enhanced CO_2 conversion by reverse water gas shift chemical looping, *J. CO2 Util.*, 2022, **56**, 101845.

45 Y. A. Daza, D. Maiti, B. J. Hare, V. R. Bhethanabotla and J. N. Kuhn, More Cu, more problems: decreased CO_2 conversion ability by Cu-doped $La_{0.75}Sr_{0.25}FeO_3$ perovskite oxides, *Surf. Sci.*, 2016, **648**, 92–99.

46 M. Lee, Y. Kim, H. S. Lim, A. Jo, D. Kang and J. W. Lee, Reverse Water–Gas Shift Chemical Looping Using a Core–Shell Structured Perovskite Oxygen Carrier, *Energies*, 2020, **13**, 5324.

47 D. Maiti, B. J. Hare, Y. A. Daza, A. E. Ramos, J. N. Kuhn and V. R. Bhethanabotla, Earth abundant perovskite oxides for low temperature CO_2 conversion, *Energy Environ. Sci.*, 2018, **11**, 648–659.

48 C. J. Bartel, C. Sutton, B. R. Goldsmith, R. Ouyang, C. B. Musgrave, L. M. Ghiringhelli and M. Scheffler, New tolerance factor to predict the stability of perovskite oxides and halides, *Sci. Adv.*, 2019, **5**, eaav0693.

49 H. Z. Shi, V. R. Bhethanabotla and J. N. Kuhn, Role of Ba in low temperature thermochemical conversion of carbon dioxide with $LaFeO_3$ perovskite oxides, *J CO_2 Util.*, 2021, **51**, 101638.

50 H. Shi, V. R. Bhethanabotla and J. N. Kuhn, Pelletized SiO_2-supported $La_{0.5}Ba_{0.5}FeO_3$ for conversion of CO_2 to CO by a reverse water–gas shift chemical looping process, *J. Ind. Eng. Chem.*, 2023, **118**, 44–52.

51 H. S. Lim, Y. Kim, D. Kang, M. Lee, A. Jo and J. W. Lee, Fundamental Aspects of Enhancing Low-Temperature CO_2 Splitting to CO on a Double La_2NiFeO_6 Perovskite, *ACS Catal.*, 2021, **11**, 12220–12231.

52 Y. Qiu, L. Ma, D. Zeng, M. Li, D. Cui, Y. Lv, S. Zhang and R. Xiao, Efficient CO_2 to CO conversion at moderate temperatures enabled by the cobalt and copper co-doped ferrite oxygen carrier, *J. Energy Chem.*, 2020, **46**, 123–132.

53 L. Ma, Y. Qiu, M. Li, D. Cui, S. Zhang, D. Zeng and R. Xiao, Spinel-Structured Ternary Ferrites as Effective Agents for Chemical Looping CO_2 Splitting, *Ind. Eng. Chem. Res.*, 2020, **59**, 6924–6930.

54 J. Rojas, E. Sun, G. Wan, J. Oh, R. Randall, V. Haribal, I.-h. Jung, R. Gupta and A. Majumdar, Iron-Poor Ferrites for Low-Temperature CO_2 Conversion *via* Reverse Water–Gas Shift Thermochemical Looping, *ACS Sustain. Chem. Eng.*, 2022, **10**, 12252–12261.

55 M. Wenzel, N. V. R. Aditya Dharanipragada, V. V. Galvita, H. Poelman, G. B. Marin, L. Rihko-Struckmann and K. Sundmacher, CO production from CO_2 *via* reverse water–gas shift reaction performed in a chemical looping mode: kinetics on modified iron oxide, *J. CO2 Util.*, 2017, **17**, 60–68.
56 M. Lee, Y. Kim, H. S. Lim, A. Jo, D. Kang and J. W. Lee, Low temperature CO_2 conversion facilitated by the preserved morphology of metal oxide-perovskite composite, *Chem. Eng. J.*, 2022, **437**, 135151.
57 D. Zeng, Y. Qiu, L. Ma, M. Li, D. Cui, S. Zhang and R. Xiao, Tuning the Support Properties toward Higher CO_2 Conversion during a Chemical Looping Scheme, *Environ. Sci. Technol.*, 2020, **54**, 12467–12475.
58 J. I. Makiura, T. Higo, Y. Kurosawa, K. Murakami, S. Ogo, H. Tsuneki, Y. Hashimoto, Y. Sato and Y. Sekine, Fast oxygen ion migration in Cu-In-oxide bulk and its utilization for effective CO_2 conversion at lower temperature, *Chem. Sci.*, 2020, **12**, 2108–2113.
59 K. Kang, S. Kakihara, T. Higo, H. Sampei, K. Saegusa and Y. Sekine, Equilibrium unconstrained low-temperature CO_2 conversion on doped gallium oxides by chemical looping, *Chem. Commun.*, 2023, **59**, 11061–11064.
60 J. I. Makiura, S. Kakihara, T. Higo, N. Ito, Y. Hirano and Y. Sekine, Efficient CO_2 conversion to CO using chemical looping over Co-In oxide, *Chem. Commun.*, 2022, **58**, 4837–4840.
61 A. More, S. Bhavsar and G. Veser, Iron–Nickel Alloys for Carbon Dioxide Activation by Chemical Looping Dry Reforming of Methane, *Energy Technol.*, 2016, **4**, 1147–1157.
62 A. More and G. Veser, Physical mixtures as simple and efficient alternative to alloy carriers in chemical looping processes, *AIChE J.*, 2017, **63**, 51–59.
63 P. T. Krenzke, J. R. Fosheim and J. H. Davidson, Solar fuels *via* chemical-looping reforming, *Sol. Energy*, 2017, **156**, 48–72.
64 X. Zhang, C. Pei, X. Chang, S. Chen, R. Liu, Z. J. Zhao, R. Mu and J. Gong, FeO_6 Octahedral Distortion Activates Lattice Oxygen in Perovskite Ferrite for Methane Partial Oxidation Coupled with CO_2 Splitting, *J. Am. Chem. Soc.*, 2020, **142**, 11540–11549.
65 D. Sastre, D. P. Serrano, P. Pizarro and J. M. Coronado, Chemical insights on the activity of $La_{1-x}Sr_xFeO_3$ perovskites for chemical looping reforming of methane coupled with CO_2-splitting, *J. CO2 Util.*, 2019, **31**, 16–26.
66 A. Riaz, T. Tsuzuki, F. Kremer, S. Sattayaporn, M. U. Ali, W. Lipiński and A. Lowe, Structural Rearrangement in LSM Perovskites for Enhanced Syngas Production *via* Solar Thermochemical Redox Cycles, *ACS Catal.*, 2020, **10**, 8263–8276.
67 X. Xia, W. Chang, S. Cheng, C. Huang, Y. Hu, W. Xu, L. Zhang, B. Jiang, Z. Sun, Y. Zhu and X. Wang, Oxygen Activity Tuning *via* FeO_6 Octahedral Tilting in Perovskite Ferrites for Chemical Looping Dry Reforming of Methane, *ACS Catal.*, 2022, **12**, 7326–7335.
68 W. Yu, X. Wang, Y. Liu, J. Wei and J. Zhang, Effect of Composition on the Redox Performance of Strontium Ferrite Nanocomposite, *Energy Fuels*, 2020, **34**, 8644–8652.
69 D. Sastre, C. Á. Galván, P. Pizarro and J. M. Coronado, Enhanced performance of CH_4 dry reforming over $La_{0.9}Sr_{0.1}FeO_3$/YSZ under chemical looping conditions, *Fuel*, 2022, **309**, 122122.
70 Y. Zhu, N. Jin, R. Liu, X. Sun, L. Bai, H. Tian, X. Ma and X. Wang, Bimetallic $BaFe_2MAl_9O_{19}$ (M = Mn, Ni, and Co) hexaaluminates as oxygen carriers for chemical looping dry reforming of methane, *Appl. Energy*, 2020, **258**, 114070.
71 Y. Zhu, W. Liu, X. Sun, X. Ma, Y. Kang, X. Wang and J. Wang, La-hexaaluminate for synthesis gas generation by Chemical Looping Partial Oxidation of Methane Using CO_2 as Sole Oxidant, *AIChE J.*, 2018, **64**, 550–563.
72 Z. Cheng, L. Zhang, N. Jin, Y. Zhu, L. Chen, Q. Yang, M. Yan, X. Ma and X. Wang, Effect of calcination temperature on the performance of hexaaluminate supported CeO_2 for chemical looping dry reforming, *Fuel Process. Technol.*, 2021, **218**, 106873.
73 L. S. Fan, L. Zeng and S. Luo, Chemical-looping technology platform, *AIChE J.*, 2015, **61**, 2–22.
74 Y. Ge, T. He, Z. Wang, D. Han, J. Li, J. Wu and J. Wu, Chemical looping oxidation of CH_4 with 99.5% CO selectivity over V_2O_3-based redox materials using CO_2 for regeneration, *AIChE J.*, 2020, **66**, e16772.
75 J. Zhang, V. Haribal and F. Li, Perovskite nanocomposites as effective CO_2-splitting agents in a cyclic redox scheme, *Sci. Adv.*, 2017, **3**, e1701184.
76 M. Tang, K. Liu, D. M. Roddick and M. Fan, Enhanced lattice oxygen reactivity over Fe_2O_3/Al_2O_3 redox catalyst for chemical-looping dry (CO_2) reforming of CH_4: synergistic La-Ce effect, *J. Catal.*, 2018, **368**, 38–52.
77 Y. Sun, J. Li and H. Li, Core–shell-like Fe_2O_3/MgO oxygen carriers matched with fluidized bed reactor for chemical looping reforming, *Chem. Eng. J.*, 2022, **431**, 134173.
78 S. Assabumrungrat, S. Charoenseri, N. Laosiripojana, W. Kiatkittipong and P. Praserthdam, Effect of oxygen addition on catalytic performance of $Ni/SiO_2 \cdot MgO$ toward carbon dioxide reforming of methane under periodic operation, *Int. J. Hydrogen Energy*, 2009, **34**, 6211–6220.
79 K. Otsuka, Y. Wang, E. Sunada and I. Yamanaka, Direct Partial Oxidation of Methane to Synthesis Gas by Cerium Oxide, *J. Catal.*, 1998, **175**, 152–160.
80 J. Wei and E. Iglesia, Structural and Mechanistic Requirements for Methane Activation and Chemical Conversion on Supported Iridium Clusters, *Angew. Chem., Int. Ed.*, 2004, **43**, 3685–3688.
81 Y. Mao, L. Zhang, X. Zheng, W. Liu, Z. Cao and H. Peng, Coke-resistance over Rh–Ni bimetallic catalyst for low temperature dry reforming of methane, *Int. J. Hydrogen Energy*, 2023, **48**, 13890–13901.
82 V. P. Haribal, X. Wang, R. Dudek, C. Paulus, B. Turk, R. Gupta and F. Li, Modified Ceria for "Low-Temperature" CO_2 utilization: A Chemical Looping Route to Exploit Industrial Waste Heat, *Adv. Energy Mater.*, 2019, **9**, 1901963.
83 A. Löfberg, J. Guerrero-Caballero, T. Kane, A. Rubbens and L. Jalowiecki-Duhamel, Ni/CeO_2 based catalysts as oxygen vectors for the chemical looping dry reforming of methane

for syngas production, *Appl. Catal. B Environ.*, 2017, **212**, 159–174.

84 Y. Han, M. Tian, C. Wang, Y. Kang, L. Kang, Y. Su, C. Huang, T. Zong, J. Lin, B. Hou, X. Pan and X. Wang, Highly Active and Anticoke Ni/CeO_2 with Ultralow Ni Loading in Chemical Looping Dry Reforming *via* the Strong Metal–Support Interaction, *ACS Sustain. Chem. Eng.*, 2021, **9**, 17276–17288.

85 S. Miyazaki, Z. Li, Z. Maeno, T. Toyao, M. Ito, Y. Nakajima and K. Shimizu, Operando Ce *K*-edge XANES Study of Low-loading Ni/CeO_2 in Chemical Looping Dry Reforming of Methane, *Chem. Lett.*, 2022, **51**, 914–918.

86 J. Guerrero-Caballero, T. Kane, N. Haidar, L. Jalowiecki-Duhamel and A. Löfberg, Ni, Co, Fe supported on Ceria and Zr doped Ceria as oxygen carriers for chemical looping dry reforming of methane, *Catal. Today*, 2019, **333**, 251–258.

87 J. Wang, K. Li, H. Wang, Z. Li and X. Zhu, Sandwich Ni-phyllosilicate@doped-ceria for moderate-temperature chemical looping dry reforming of methane, *Fuel Process. Technol.*, 2022, **232**, 107268.

88 S. Miyazaki, Z. Li, L. Li, T. Toyao, Y. Nakasaka, Y. Nakajima, K. Shimizu and Z. Maeno, Chemical Looping Dry Reforming of Methane over Ni-Modified WO_3/ZrO_2: Cooperative Work of Dispersed Tungstate Species and Ni over the ZrO_2 Surface, *Energy Fuels*, 2023, **37**, 7945–7957.

89 Z. Maeno, H. Koiso, T. Shitori, K. Hiraoka, S. Seki and N. Namiki, Syngas Production by Chemical Looping Dry Reforming of Methane over Ni-modified MoO_3/ZrO_2, *Chem.–Asian J.*, 2023, e202301096.

90 F. R. García-García and I. S. Metcalfe, Chemical looping dry reforming of methane using mixed oxides of iron and cerium: operation window, *Catal. Commun.*, 2021, **160**, 106356.

91 L. S. Fan, S. Luo and L. Zeng, *US Pat.*, US10501318B2, 2018.

92 L. S. Fan, S. Luo, L. Zeng and D. Xu, *High Quality Syngas Production Using Composite Metal Oxides*, US Provisional Patent Application, 2013.

93 S. Luo, L. Zeng and L. S. Fan, Chemical Looping Technology: Oxygen Carrier Characteristics, *Annu. Rev. Chem. Biomol. Eng.*, 2015, **6**, 53–75.

94 Y. Song, S. Teng, † D. Fang, Y. Lu, Z. Chen, R. Xiao and D. Zeng, Machine Learning for Chemical Looping: Recent Advances and Prospects, *Energy Fuels*, 2024, **38**, 11541–11561.